

Indirect measurements of the composition of ultrafine particles in the Arctic late-winter

Deanna C. Myers¹, Michael J. Lawler¹, Roy L. Mauldin², Steven Sjostedt³, Manvendra Dubey⁴,
Jonathan Abbatt⁵, James N. Smith¹

¹Department of Chemistry, University of California, Irvine, CA, 92697, USA

²Department of Atmospheric and Oceanic Sciences, University of Colorado, Boulder, CO, 80309, USA

³Morgan Community College, Fort Morgan, CO, 80701, USA

⁴Los Alamos National Laboratory, Los Alamos, NM, 87545, USA

⁵Department of Chemistry, University of Toronto, Toronto, Ontario, M5S 3H6, Canada

Abstract

We present indirect measurements of size-resolved ultrafine particle composition conducted during the Ocean–Atmosphere–Sea Ice–Snowpack (OASIS) Campaign in Utqiagvik, Alaska, during March 2009. This study focuses on measurements of size-resolved particle hygroscopicity and volatility measured over two periods of the campaign. During a period that represents background conditions in this location, particle hygroscopic growth factors (HGF) at 90% relative humidity ranged from 1.45–1.51, which combined with volatility measurements suggest a mixture of ~30% ammoniated sulfates and ~70% oxidized organics. Two separate regional ultrafine particle growth events were also observed during this campaign. Event 1 coincided with elevated levels of H₂SO₄ and solar radiation. These particles were highly hygroscopic (HGF=2.1 for 35 nm particles), but were almost fully volatilized at 160 °C. The air masses associated with both events originated over the Arctic Ocean. Event 1 was influenced by the upper marine boundary layer, while Event 2 spent more time closer to the surface and over open ocean leads, suggesting marine influence in growth processes. Event 2 particles were slightly less hygroscopic (HGF=1.94 for 35nm and 1.67 for 15nm particles), and similarly volatile. We hypothesize that particles formed during both events contained 60–70% hygroscopic salts by volume, with the balance for Event 1 being sulfates and oxidized organics for Event 2. These observations suggest that primary sea spray may be an important initiator of ultrafine particle formation events in the Arctic late-winter, but a variety of processes may be responsible for condensational growth.

1 Introduction

Aerosol particles in the Arctic are known to exhibit seasonal variability in their chemical and physical properties. In many high-latitude regions, winter and early spring are dominated by Arctic Haze, a phenomenon characterized by long-range transport of anthropogenic pollutants and resulting in the highest mass concentrations of particulate matter (Barrie, 1986; Rahn, 1981; Tunved et al., 2013). Accumulation mode particles dominate during this period, largely from transport of anthropogenic pollution originating from Eurasia (Barrie, 1986; Frossard et al., 2011; Heintzenberg, 1982; Law & Stohl, 2007; Quinn et al., 2017; Rahn, 1981; Tunved et al., 2013). A persistent boundary layer effectively traps pollution over the Arctic, coastal Eurasia, and much of Canada until late spring, when it recedes to polar north (Barrie, 1986). Late spring and summer are less anthropogenically-influenced, and thus are characterized by lower particle concentrations (Browse et al., 2012; Croft et al., 2016; Garrett et al., 2011; Ström et al., 2003; Tunved et al., 2013). During that period, marine biogenic emissions and photochemistry are key drivers of atmospheric chemistry (Dall'Osto, et al., 2018; Quinn et al., 2002; Tunved et al., 2013).

Several recent studies have shown that the formation and growth of sub-100 nm diameter ultrafine particles (UFP) occur readily in the Arctic atmosphere (Allan et al., 2015; Asmi et al., 2016; Baccarini et al., 2020; Chang et al., 2011; Collins et al., 2017; Dall'Osto et al., 2017; Dall'Osto et al., 2018; Giamarelou et al., 2016; Heintzenberg et al., 2015; Karl et al., 2013, 2012; Kecorius et al., 2019; Kolesar et al., 2017; Kupiszewski et al., 2013; Nguyen et al., 2016; Tunved et al., 2013; Willis et al., 2016; Ziemba et al., 2010). However, few to date have focused on the composition of Arctic UFP and most observations have occurred during summer. Prior spring and summer studies have attributed UFP formation events to photochemical sulfuric acid (H_2SO_4) production (Covert & Heintzenberg, 1993), with sulfate considered an important particle component (Nyeki et al., 2005; Wiedensohler et al., 1996). These employed filters and impactors for offline chemical analysis, biasing these results to larger particles that may not represent the composition of UFPs. Size-resolved nanoparticle composition of Arctic UFPs has been studied using mostly indirect measurements, with a focus on formation and growth events during late spring and summer. In the Canadian Arctic, UFP formation was observed to occur freely in the marine boundary layer, with complementary gas-phase measurements suggesting marine biogenic sources of organic and sulfur-containing gas-phase precursors (Burkart et al., 2017). Several observations of UFP formation and growth from other Arctic locations associated these phenomena with oxidized products of dimethylsulfide (DMS) like methanesulfonic acid (MSA) and H_2SO_4 , suggesting a marine biogenic influence (Abbatt et al., 2019; Chang et al., 2011; Dall'Osto et al., 2018; Ferek et al., 1995; Ghahremaninezhad et al., 2016; Leaitch et al., 2013; Quinn et al., 2002). Indirect measurements of

summertime particle composition in Ny-Alesund, Svalbard, indicated that organic vapor condensation plays a large role in UFP formation (Kecorius et al., 2019). Organic compounds were found to contribute to the growth of newly formed UFPs in the Canadian Arctic, with a small contribution from sulfur-containing compounds (Tremblay et al., 2019). Willis et al., (2016) showed that growth of sub-20 nm particles to ~50 nm coincided with the presence of organics, trimethylamine, and MSA in particles 80 nm and larger, suggesting the particles grew by condensation of MSA and other lower-volatility organic species. Model results from Canadian Arctic observations using a paired chemical transport-microphysics model indicate that ternary nucleation from H₂SO₄, ammonia (NH₃), and water, followed by condensation from marine biogenic species and biogenically derived sulfur compounds, accounts for more than 90% of the simulated number concentration for particles larger than 20 nm (Croft et al., 2019). Other measurements performed in late-summer suggest that iodine (Allan et al., 2015; Baccarini et al., 2020) and marine nanogels are responsible for some observed UFP formation events (Dall'Osto et al., 2017; Karl et al., 2013; C Leck et al., 2013; Caroline Leck & Bigg, 2010). Measurements made during 11 particle formation events aboard the Swedish icebreaker *Oden* in August and September of 2018 found that these events coincided with elevated levels of iodic acid (HIO₃) and relatively low levels of H₂SO₄ (Baccarini et al., 2020). Fragmentation of primary marine biological particles, where nano-granules are released from evaporation of cloud/fog droplets while H₂SO₄ nucleates to form clusters, both grow through condensation of low-volatility vapors, and then coagulate to form particles larger than 3nm, has been proposed to explain numerous UFP formation events observed in the high Arctic during late spring and summer (Karl et al., 2013). Taken together, these results suggest gas-phase ammonia, amines, organics, oxidized sulfur species, and fragmentation of primary marine particles contribute to the formation and growth of UFPs in the late spring and early summer in this region.

Winter and early spring measurements of UFP formation events and the composition of these particles are largely missing. This is due in part to the dominant accumulation mode that biases bulk and sub-micron measurements towards larger particles. Some insights into the mechanisms of UFP formation can nonetheless be gained through such measurements. Analysis of sub-micron aerosol particle composition during particle formation events in Tiksi, Siberia, made by aerosol mass spectrometry (AMS) found that while summertime events were driven by oxidation of biogenic low-volatility gases, early spring events are likely due to oxidation of anthropogenic precursors of Arctic Haze (Asmi et al., 2016). Filter samples have shown submicron particles are largely composed of sea salt and non-sea-salt sulfates (nss sulfate) (Kirpes et al., 2018, 2019; Patterson et al., 1967; Quinn et al., 2002; Tomasi et al., 2012). Long-term measurements taken at Utqiagvik (formerly Barrow), Alaska are consistent with other measurements indicating nss sulfate is a major component of submicron wintertime aerosol, but the concentration decreased by ~60% between 1976 and 2008. Elemental analysis indicated that while source

regions remained the same over this time period, emissions decreased (Quinn et al., 2009). Soot particle AMS (SP-AMS) measurements made in Greenland have linked UFP formation in February through May to MSA and molecular iodine, suggesting contributions from both biotic and abiotic sources (Dall'Osto, et al., 2018). Since most winter-time measurements to date have been performed on bulk aerosol, Arctic UFP composition is still not understood in the winter and early spring. More measurements are needed in order to understand the mechanisms by which new particles form in this important region.

We seek to address this measurement gap by reporting indirect measurements of UFP composition made during the Ocean – Atmosphere – Sea Ice – Snowpack (OASIS) Campaign in Utqiagvik, Alaska during March 2009. A period from 27 – 31 March was determined to have winds from the Arctic Ocean, with particle properties measured during this time representing background conditions. Two separate nanoparticle growth events were observed during this that campaign (12 -14 March), where particles grew from 5 nm to ~ 20 nm in diameter. Size-resolved hygroscopicity and volatility measured during these events were analyzed to hypothesize the species involved the growth of these newly formed particles.

2 Methods

2.1 Site description

Measurements were made during the OASIS field campaign in Utqiagvik, Alaska during March and April 2009. The focus of this paper is on two periods – one that featured measurements of two separate UFP growth events occurring during 12 – 14 March, and a second background period from 27 – 31 March. All times are reported in Alaska Daylight Time (AKDT; UTC – 8 hours) and are referred to as “local time” in this work. Particle measurements were collected in a Quonset hut at the U.S. Navel Arctic Research Laboratory (NARL) and trace gas and surface meteorology measurements were performed approx. 1 km away in buildings located near the Barrow Arctic Research Center (BARC). Numerous measurements of key trace gases and particle properties, as well as of meteorology, were made over the course of the campaign; those pertinent during the time periods of interest are outlined below.

2.2 Air mass origin and station meteorology

Air mass backward trajectories were calculated to determine source influences for each of the ultrafine particle events observed using the NOAA Hybrid Single-Particle Lagrangian Integrated Trajectory (HYSPLIT) transport model (Rolph et al., 2017; Stein et al., 2015). Backward trajectories of 72-hour duration were determined for air masses arriving 50 meters above ground level (AGL) at the measurement site at the beginning and halfway through the UFP events (Event 1: 3/12/09 04:07 – 19:02

ADT; Event 2: 3/13/09 20:37 – 3/14/09 3:47 ADT) using the Global Data Assimilation System (GDAS) 1° meteorology. Satellite images from NASA Moderate Resolution Imaging Spectroradiometer (MODIS)/Aqua Sea Ice Extent with temporal resolution of 5 minutes and spatial resolution of 1 kilometer were used to identify leads and areas of open water in the sea ice (Hall & Riggs, 2015). Images were analyzed for 10 – 14 March, corresponding to the timespan of the HYSPLIT back trajectories calculated for each UFP growth event observed.

Sonic anemometers (Applied Technologies, Sonic Anemometer/Thermometer model SATI/3K) were used to measure three-dimensional wind velocities at 10 Hz. Wind speed and direction were obtained from vector-averaging the horizontal wind velocities over 1-minute intervals and are accurate to $\pm 0.03 \text{ m s}^{-1}$ and $\pm 0.1^\circ$, respectively. Wind direction data are color-coded to identify periods with likely local influences at the measurement sites (labelled “Utqiagvik”, “local building” and “local NNW”) and periods with minimal local influence (labelled “clean”). Time periods with “calm” winds were those with minimal wind.

Solar radiation was measured at the NOAA Barrow Atmospheric Baseline Observatory, approximately 3.5 km northeast of NARL. We report 1-minute measurements of downwelling global solar radiation (W m^{-2}), performed with an unshaded Precision Spectral Pyranometer (Eppley).

2.3 Particle physical, chemical, and radiative properties

2.3.1 Particle number size distributions

Particle number size distributions for particles with electrical mobility diameter of 4 nm to 1 μm were collected using a particle size distribution system consisting of 3 instruments that measure with a 5-minute time resolution. A nanometer scanning mobility particle sizer (nano-SMPS) comprised of a home-built bipolar neutralizer, a TSI model 3085 Differential Mobility Analyzer (DMA), a home-built high voltage and flow control system, and an Ultrafine Condensation Particle Counter (UCPC, TSI model 3025a), covered the particle mobility range of 4 to 30 nm. A scanning mobility particle sizer (SMPS), identical to the nano-SMPS except for the use of a TSI model 3081 DMA and a standard condensation particle counter (CPC, TSI model 7620, modified to run at 1.2 lpm aerosol flow rate), measured particles of diameter ~22 to ~225 nm. An optical particle counter (OPC, Lasair model 1002 PMS, Inc.) measured particle number-size distributions over the diameter range of 0.1 to 1 μm . Measured distributions were combined to create a continuous size distribution, which was used also in calculations of particle growth rates following the method outlined in Dal Maso et al. (2005) and gamma (Γ ; Section 3.3) (Kuang et al., 2010). Size distributions were corrected for the transmission efficiency of the inlet tubing using

theoretically predictions that assume laminar flow, the latter of which was confirmed by our inlet flow rate measurements (Hinds, 1999).

2.3.2 Particle optical properties

Bulk ambient particle absorption and scattering coefficients were measured at 781 nm using a photoacoustic soot spectrometer (PASS-1, Droplet Measurement Technologies using principles and protocols described in Flowers et al. (2010). Aerosol particle absorption coefficients (β_{abs}) at 781 nm were directly measured using the photoacoustic technique and scattering coefficients (β_{sca}) were measured simultaneously on the same dry aerosol sample with an integrating nephelometer. Noise was removed from collected data using a bandpass filter, with a band set between 0 and 12 M m⁻¹ for scattering data, and 0 and 30 M m⁻¹ for the absorption data. The instrument was zeroed every 40 minutes to eliminate systematic drifts and the reported measurements were averaged in 150 second bins to enhance signal to noise. Particle single scattering albedo (SSA) was calculated as follows:

$$SSA = \frac{\beta_{sca}}{\beta_{sca} + \beta_{abs}} \quad (1)$$

Calculated values of SSA were used to determine the relative absorbing versus scattering properties of bulk particles during periods of interest and were also used to identify periods of local pollution such as that provided by snow removal equipment that have low SSA due to absorbing soot emissions, which would not have been identified from wind direction measurements.

2.3.3 Indirect measurements of particle chemical properties

A hygroscopicity tandem differential mobility analyzer (HTDMA) measured the hygroscopic growth factor of size-selected particles at 90% relative humidity (RH). In this home-built instrument, which is also described in detail elsewhere (Lance et al., 2013), particles were neutralized with a unipolar neutralizer, dried to ~2% RH, and then size-selected by the first DMA (home-built, but identical in design to TSI model 3081). Dry particle sizes studied had electrical mobility diameters ($Dp(RH_{dry})$) of 15, 35, 50, 75, and 110 nm. Size-selected particles then passed to the conditioning chamber, where they were exposed to a controlled 90% RH. The resulting size distribution was measured by a second, identical DMA and a CPC (TSI model 3010). Sheath and excess flows in the DMAs were 5 lpm with an aerosol flow of 0.6 lpm. Data was corrected for variations in relative humidity in the second DMA using methods outlined in Gysel et al. (2009) and Keith and Arons (1954). All corrected size distributions during the periods discussed below consisted of a single mode, suggesting internally mixed aerosol. These size distributions were fitted with a Gaussian curve and the peak of the curve was used to represent the peak diameter of the humidified mode $Dp(RH_{humid})$. Hygroscopic growth factor (HGF) was calculated using:

$$HGF = \frac{Dp(RH_{humid})}{Dp(RH_{dry})} \quad (2)$$

From measurements of HGF , we then estimate the volume fraction of representative particulate compounds using the Zdanovskii-Stokes-Robinson (ZSR) relation:

$$HGF_{meas} = (\sum_k \varepsilon_k HGF_k^3)^{1/3}$$

where ε_k is the volume fraction of pure component k in the particle and HGF_k is the growth factor of pure component k (Malm & Kreidenweis, 1997; Stokes & Robinson, 1966).

A volatility TDMA (VTDMA) measured the volatility of size-selected particles at different temperatures. Ambient particles were neutralized and size-selected by the first DMA (TSI model 3081) at mobility diameters of 15, 35, 75, 110, and 165 nm. Particles then passed through a fast stepping/scanning thermodenuder built by Aerodyne Research, Inc., and modeled after the system described by Huffman et al. (2008). The thermodenuder was stepped at temperatures of $T_D = 30, 40, 80, \text{ and } 160^\circ\text{C}$, and time was allowed during each step for the temperature to stabilize before measurement. The particle number size distribution was measured with the second DMA (TSI model 3081) and CPC (TSI model 3010). The sample flow rate through the denuder was set to 0.6 LPM, which was determined to be optimal for this design by Wehner et al. (2002). Like the HTDMA, sheath flows in the DMAs were 5 lpm with a particle flow of 0.6 lpm. Data are reported at each temperature as the volume fraction remaining, VFR , which is defined as:

$$VFR = \frac{V_T}{V_{30^\circ\text{C}}} \quad (3)$$

where V_T is the integrated total particulate volume (assuming spherical particles) at temperature, T . We note that ambient atmospheric temperatures during the measurement periods generally ranged from -20 to -30°C while the VTDMA maintained a temperature within the Quonset hut of $\sim 14^\circ\text{C}$, likely leading to evaporation of some particulate compounds prior to the initial size-selection. For this reason, and because the Quonset hut temperature was poorly controlled, we chose to divide V_T by the integrated volume of particles exposed to our lowest controlled temperature, 30°C ($V_{30^\circ\text{C}}$), in our calculations of VFR . Prior to analysis, some instrument noise was easily identified in data as repetitive modes present throughout the sampling and calibration periods and was consequently removed.

Both the HTDMA and VTDMA were calibrated at the site, before and after the observation period, using ammonium sulfate aerosol that was aerosolized using a commercial aerosol generator (TSI model 3076). These experiments confirmed that both instruments were operating properly and that no further adjustments to the data, other than those described above, were needed.

2.4 Trace Gas Analysis

Gas-phase concentration measurements of H_2SO_4 , OH, and MSA were obtained using a selected ion chemical ionization mass spectrometer (SICIMS). Measurements were made using an inlet ~ 1.5 m above the snow surface in a building located ~ 500 m east of the particle measurement location. Details of this instrument have been previously reported in Tanner et al., (1997) and Mauldin et al., (1998). Data were calibrated and are presented as 30-second averages.

3 Results and Discussion

3.1 Campaign overview

The OASIS Campaign took place from late February through mid-April 2009, with particle measurements beginning on 5 March. The foci of the campaign were on gas-phase exchanges between the ocean, atmosphere, sea ice, and snowpack, the impact of these processes on oxidation capacity in the remote Arctic atmosphere, and how they may change with a changing climate (NCAR, 2012). The measurement period during late winter and early spring is chemically interesting because of the appearance of light at the end of polar winter (Barrie, 1986). With increasing solar radiation during the

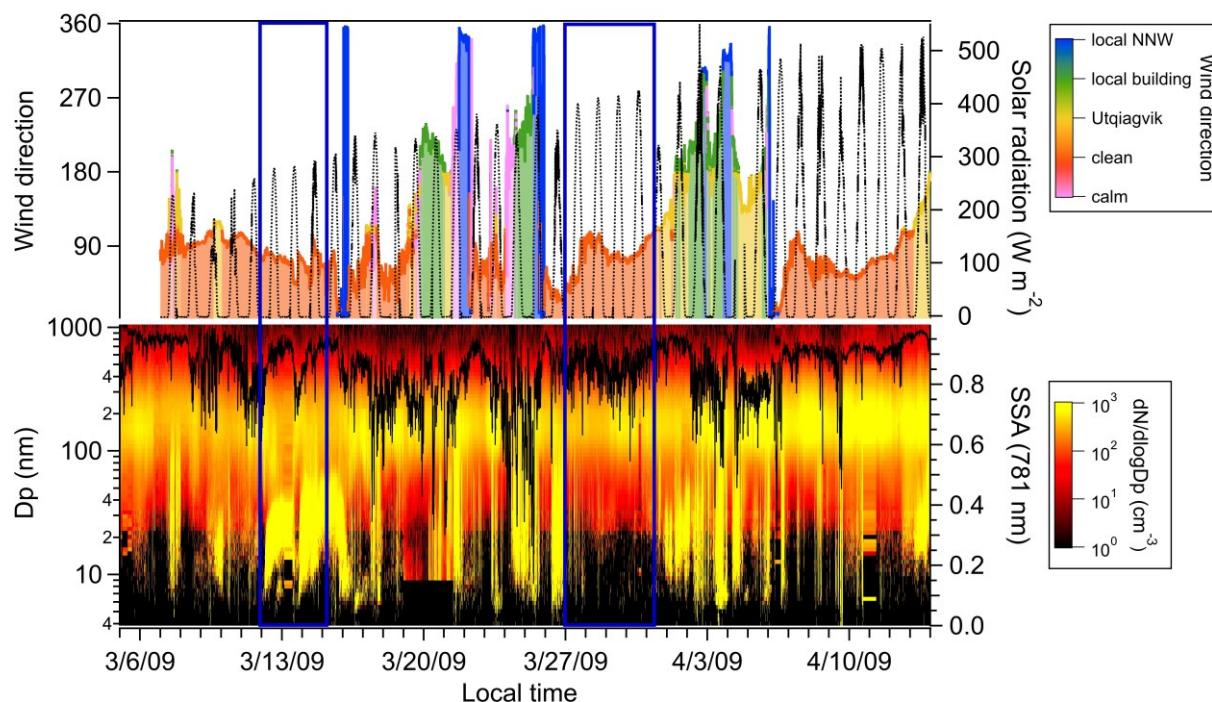


Figure 1. Meteorological data and bulk particle properties during the entire OASIS observation period. Plotted above are wind direction (color-coded to show relative direction of origin) and downwelling solar radiation. The lower plot is the particle number size distribution (diameters 4 to 1000 nm) and single scattering albedo (SSA) measured at 781 nm (black). The focus of this work is a background period (27 – 31 March) and two distinct ultrafine particle growth events (12 – 14 March), which are boxed in blue.

course of this campaign, photochemistry became progressively more important during the observation period (Fig. 1). Several major findings from OASIS have thus far related to gas-phase photochemical halogen chemistry, with a particular focus on bromine, including its efficacy in ozone (O₃) depletion compared to chlorine (Thompson et al., 2015) and its recycling process (Frieß et al., 2011; Liao et al., 2012).

Throughout the course of the campaign, there are two prominent features in the particle size distribution measurements: sub-20 nm particles appear at the site at an initial diameter of 5 nm in bursts, with no *in situ* nucleation observed at the site as evidenced by the lack of sub-5 nm diameter particles; and a continuous mode centered at 200 nm (Figure 1). Note that the campaign-averaged value of SSA is ~0.8, with decreases to values ~0.5 during periods with “local building” and “local NNW” influence (Figure 1). This indicates that local particle emissions are more highly absorbing than ambient Arctic particles in this region, which has been observed in numerous Arctic sites during this time of year (Bodhaine et al., 1981; Clarke et al., 1984; Patterson et al., 1967; Polissar et al., 2001; Tomasi et al., 2012).

3.2 Background period

We begin by reporting measurements made during a period (27 – 31 March) that we identified as “clean” in order to explore regional Arctic UFP physico-chemical properties and address the lack of winter and spring observations. Figure 2 shows a summary of the data that include, to the best of our knowledge, the first indirect composition measurements of size-selected, sub-500 nm atmospheric particles in the Utqiagvik area. Bulk SSA was, on average, 0.861 ± 0.055 , indicating internally mixed black carbon (BC) in this region, and showed relatively low variability, suggesting that local emissions did not substantially bias our measurements during this period. Like the rest of the campaign, sub-20 nm particle concentrations were very low with total number concentration during the period averaging 380 cm⁻³. In comparison to other Arctic measurements made in March, this is lower than the concentration measured in Siberia (Asmi et al., 2016), but about twice as high as that observed in Svalbard (Tunved et al., 2013) and Greenland (Nguyen et al., 2016). These differences in particle concentration exemplify the variability in particle properties throughout different Arctic locations.

Figure 2c shows *HGF* measured at 90% RH for 35, 75, and 110 nm size-selected ambient particles. Data for 15 nm particles are missing for both HTDMA and VTDMA instruments due to the extremely low concentrations of these particles. The figure also includes published *HGF* data for laboratory-generated sea salt aerosol ($D_p = 50$ nm) (Zieger et al., 2017), ammonium sulfate (Asmi et al., 2010; Hämeri et al., 2000; Sjogren et al., 2007), black carbon (Weingartner et al., 1995), and a seawater

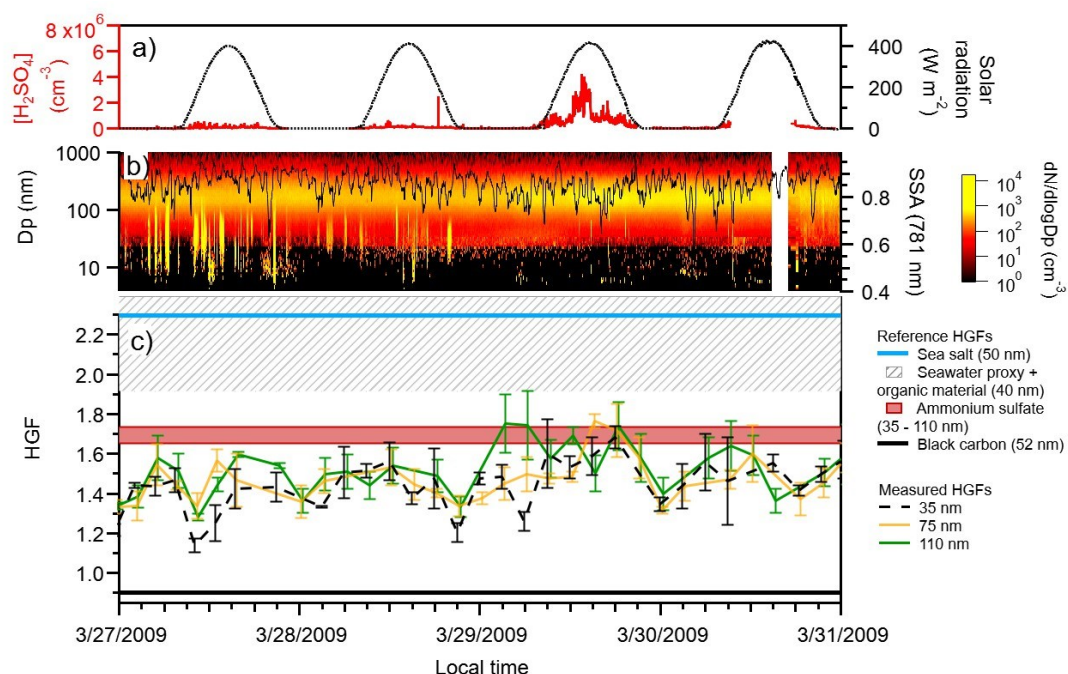


Figure 2. Particle properties measured during the background period, showing (a) H_2SO_4 concentration (red), downwelling solar radiation (black); (b) particle size distribution for particle sizes between 4 and 1000 nm in diameter, and single scattering albedo (black); and (c) measured particle growth factors for 35 nm (black, dashed), 75 nm (gold), and 110 nm (green, dashed) particles. Also plotted are reference growth factors for sea salt (light blue; Zieger et al., 2017), seawater proxy with organic material (gray hashed; Fuentes et al., 2011), ammonium sulfate (red, 35 – 110 nm size selected; Hämeri et al., 2000), and black carbon (black, Weingartner et al., 1995).

proxy containing varying amounts of organic material ($D_p = 40 \text{ nm}$) (Fuentes et al., 2011). For the duration of the background period, ambient particles were less hygroscopic than sea salt and seawater proxy references, with average *HGFs* of 1.45 ± 0.12 ($D_p = 35 \text{ nm}$), 1.48 ± 0.11 ($D_p = 75 \text{ nm}$), and 1.51 ± 0.12 ($D_p = 110 \text{ nm}$) measured. There is a small degree of size-dependence on *HGF* during this period, although the values and their respective standard deviations all lie within the same range.

Figure 3 shows the *VFR* for ambient 35, 75 and 110 nm size-selected particles. Negligible particle volume is lost at all sizes upon heating to $40 \text{ }^\circ\text{C}$ ($3.52 \pm 0.011 \%$, $3.53 \pm 0.20 \%$ and $2.54 \pm 0.78 \%$, respectively), which corresponds to the loss of higher-volatility compounds such as semivolatile organics (Burtscher et al., 2001; Häkkinen et al., 2012; Kreidenweis et al., 1998). Volume loss at $80 \text{ }^\circ\text{C}$, indicative of evaporation of lower-volatility organic species (Burtscher et al., 2001; Häkkinen et al., 2012; Kreidenweis et al., 1998) and certain higher volatility inorganic salts (Bergin et al., 1997), accounts for $80.8 \pm 0.2 \%$ of the volume for sampled 35 nm particles, $84.3 \pm 0.2 \%$ of the volume for sampled 75 nm particles and $65.7 \pm 0.9 \%$ of the volume for 110 nm sampled particles. Nearly all particle volume was lost upon heating to $160 \text{ }^\circ\text{C}$; at this temperature, $3.0 \pm 0.1 \%$ of the total volume of 35 nm size-selected particles, $2.9 \pm 0.2 \%$ of the total volume of 75 nm size-selected particles and $4.7 \pm 2.3 \%$ of the total

volume of 110 nm size-selected particles remained. This likely is BC and may explain the average SSA values measured during this time period, which indicate that BC is internally mixed in bulk aerosol.

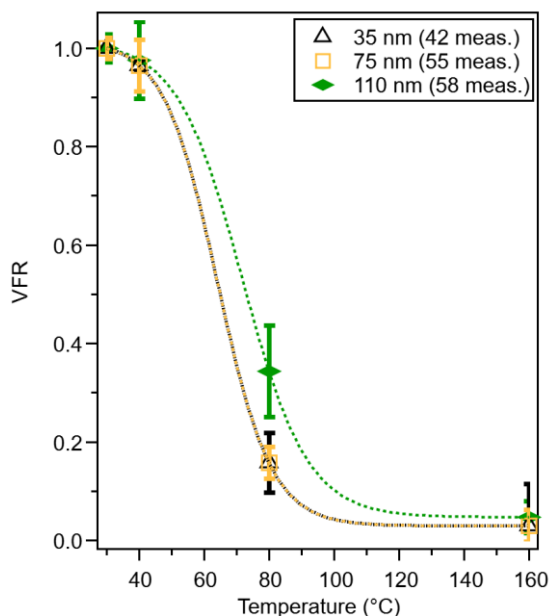


Figure 3. Average volume fraction remaining at 40, 80, and 160 °C for 35, 75 and 110 nm size-selected particles during the background period (27 – 31 March) with sigmoidal fits to data. The error bars represent standard deviation and the number of measurements at each size is shown in the legend. Initial volume ($VFR = 1$) is assumed to be the volume at 30 °C.

Combining the results of the *HGF* and *VFR* analyses provides insights into the composition of background UFPs. The high volume loss of particles at 80 °C makes it unlikely that a significant fraction of UFP volume consists of low-volatility inorganic salts. This is supported by the *HGF* analysis that shows significantly lower hygroscopicity compared to sea salt and seawater proxy reference particles (Figure 2c). The observed evaporation behavior is consistent with sulfate that is partially or fully neutralized by a base such as ammonia, which is expected to fully evaporate at temperatures below 160 °C as confirmed by our calibrations as well as those performed by Huffman et al., (2008) using a similar instrument. The measured *HGF* is slightly below than that of ammonium sulfate (Figure 2c) with the exception of a period of elevated gas phase H_2SO_4 on 29 March during which *HGF* increased slightly, supporting a contribution of sulfate to UFP

composition with the addition of a less hygroscopic material. This leads us to hypothesize that UFPs also contain some fraction of lower hygroscopicity organics. Organic compounds are routinely detected in marine aerosol (Cochran et al., 2017; O’Dowd et al., 2004; Prather et al., 2013). A mixture of organics and sulfate is also consistent with the measured *VFR* data, as loss of particulate volume over the size range of 40 – 160 °C is consistent not only with ammonium sulfate but with oxidized organics (Huffman et al., 2009). Our measurements suggest that, while it may be possible that primary organics contribute to background UFP composition, the observation that *VFR* is nearly zero at 160 °C suggests minimal contribution from low-volatility primary marine organic species (Frossard et al., 2014), and a small contribution from black carbon (Jennings et al., 1994). The measured *HGFs* may be consistent with that measured for marine nanogels (Hawkins & Russell, 2010; Ovadnevaite et al., 2011), the latter of which ranged from 1.2 to 1.3 at 90% RH.

An estimate of the volume fractions of sulfate salt and organic species, using the *HGFs* of ammonium sulfate (1.7) (Hämeri et al., 2000) and atmospheric organic matter (1.2) (Gysel et al., 2004), was performed using the average ambient *HGF* measured for each particle size reported above. Using the ZSR method with these assumptions, we estimate that, on average, volume fractions of ammonium sulfate (ϵ_{AS}) and organic species (ϵ_{ORG}) were 0.48 and 0.52 for 35 nm particles, 0.44 and 0.56 for 75 nm particles, and 0.50 and 0.50 for 110 nm particles, respectively. Estimations of volume fraction using H_2SO_4 as a third component ($HGF = 1.9$, ϵ_{SA}) were more consistent with the *VFR* measured for the larger particle sizes; for 35 nm, $\epsilon_{AS} = 0.10$, $\epsilon_{SA} = 0.20$, $\epsilon_{ORG} = 0.70$; for 75 nm, $\epsilon_{AS} = 0.10$, $\epsilon_{SA} = 0.23$, $\epsilon_{ORG} = 0.67$; and for 110 nm, $\epsilon_{AS} = 0.10$, $\epsilon_{SA} = 0.27$, $\epsilon_{ORG} = 0.63$. These estimates support the hypothesis that partially neutralized sulfate and organic species contribute mainly to the observed UFP volume.

3.3 Ultrafine particle growth events

In mid-March there were two distinct UFP growth events observed at the site occurring on consecutive days (Figure 4). Both occurred during a “clean” period and there was no evidence in SSA data (Event 1: 0.845 ± 0.076 ; Event 2: 0.857 ± 0.030) to suggest any site-specific pollution impacting the particle properties measured. Bulk particle SSA measured during both periods were very similar to both each other and the background period average. Event 1 was first observed at the site at just after 4:00 local time on 12 March, with particles appearing at a modal diameter of 11 nm. The modal diameter increased linearly over a 12-hour period to 21 nm, corresponding to a growth rate $0.862 \pm 0.034 \text{ nm h}^{-1}$. This event coincided with solar radiation at the site and an average measured H_2SO_4 concentration of $3.7 \times 10^6 \text{ molecules cm}^{-3}$. Event 2 was first observed at the site on 13 March at 20:40, with a measured modal diameter of 7 nm. Growth lasted for ~4 hours ending at 15 nm and a measured modal growth rate of $2.12 \pm 0.07 \text{ nm h}^{-1}$. This mode persisted after midnight, but no longer displayed growth. The event occurred at nighttime, thus solar radiation was minimal and the average concentration of H_2SO_4 was $3.0 \times 10^5 \text{ molecules cm}^{-3}$, which is close to the SICIMS lower limit of detection.

A prior analysis of ultrafine particle growth rates observed at the NOAA Research Station at Utqiagvik characterized these two growth events as “marine influenced” along with possible influence from Prudhoe Bay (Kolesar et al., 2017). To provide additional insights into the origins of these air masses, 72-hour HYSPLIT back trajectories were calculated for the period of each event before their arrival at the measurement site and are overlaid over MODIS satellite images of the region in Figure 5. There were no significant changes in the sea ice in this region over the time periods of the back trajectories, so the satellite image shown, while from 11 March, is representative of the entire modeling period (10 – 14 March). Two traces are shown for each event, with the starting point of the back trajectory corresponding to the beginning and halfway time points of the events. The black boxes on

349 Figure 5 indicate areas of direct ocean-atmosphere interfaces in the sea ice, both in the form of open
 350 leads, which are small regions of water between ice sheets that serve as direct interfaces between the

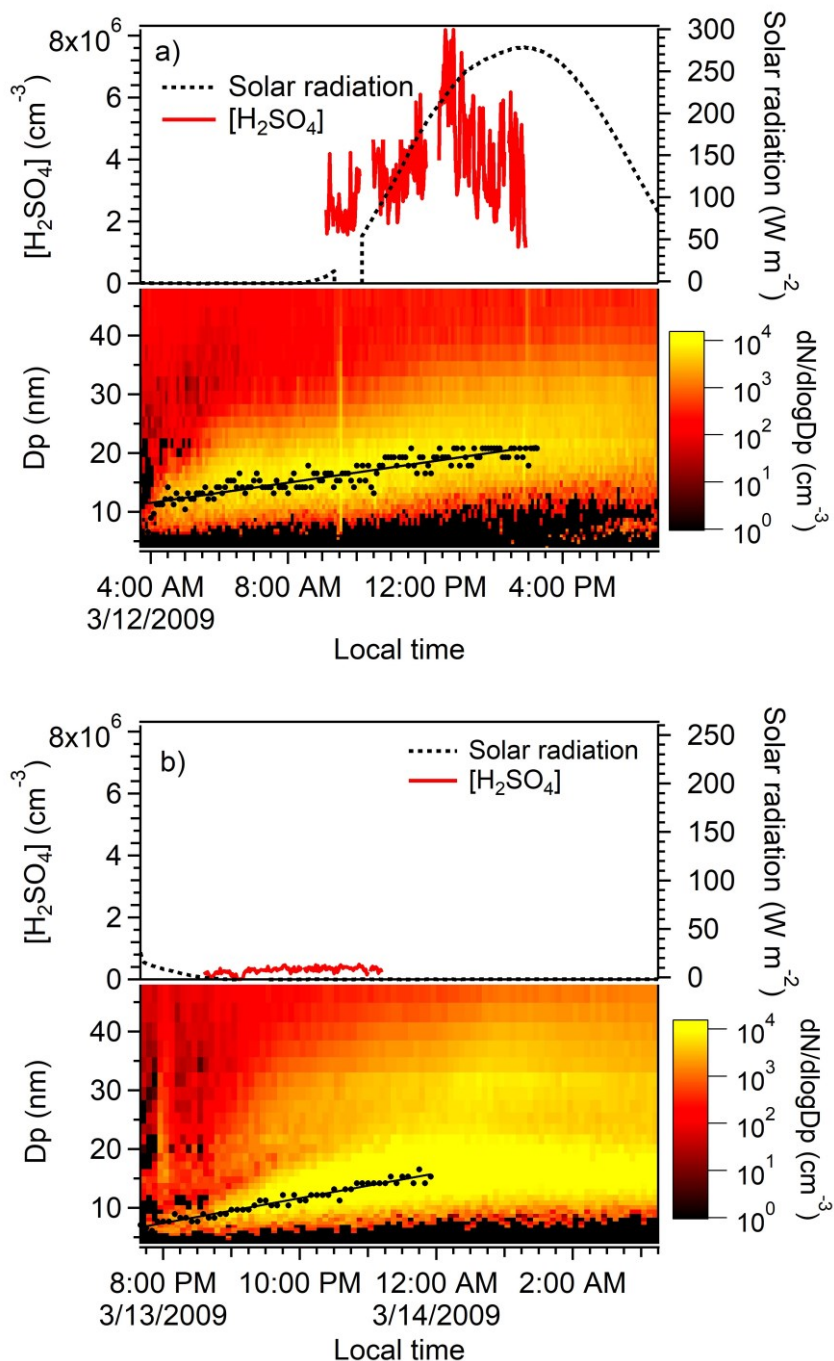


Figure 4. Photochemical and particle size distribution properties during ultrafine particle growth (a) Event 1 and (b) Event 2. Plotted are the gas-phase concentrations of H_2SO_4 (red, molecules cm^{-3}) and downwelling solar radiation (black dashes, W m^{-2}). Particle number size distributions for each growth event are shown with the mode diameter during the growth period and its linear regression fit to determine growth rates are shown in black.

351 ocean and atmosphere, and open ocean. Sea ice leads have been shown to contribute to sea spray and
 352 seawater-like particles in the atmosphere (May et al., 2016; Nilsson et al., 2001). The back trajectories for
 353 the air masses associated with both events originate in the same region of the Arctic Ocean, however there
 354 are differences in their geographic paths and altitudes. The air masses associated with Event 1 did not
 355 pass over the leads offshore of Prince Patrick Island (Northwest Territories, Canada) and spent more time

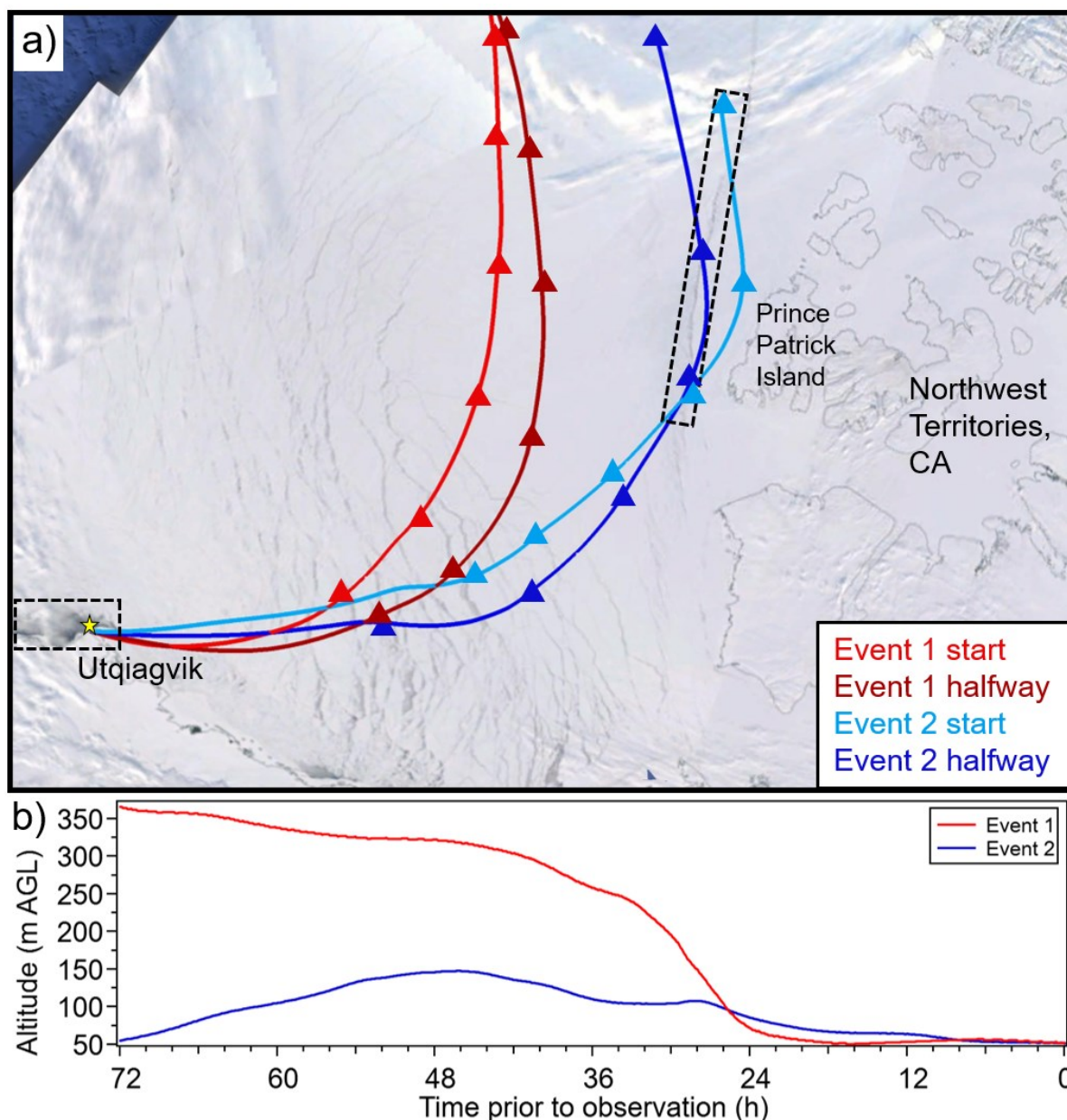


Figure 5. Air mass back trajectory analysis for each growth event. (a) HYSPLIT 72-hour back trajectories for each event plotted with MODIS satellite images from 3/11, with one trajectory at the beginning of each event and one halfway through growth. Triangles mark 12-hour time points. The blue region in the upper-left corner is an imaging artefact and does not represent open ocean. Black boxes highlight regions with sea ice leads. (b) Average altitudes above ground level (AGL) of the two trajectories calculated for each event.

aloft, at ~350 m above ground level (AGL) which near the top of the estimated boundary layer during this time (Boylan et al., 2014), reaching surface level 24 hours before the start of the observed event. The air masses impacting Event 2 passed over open leads off Prince Patrick Island and are much closer to the surface (not exceeding 150 m AGL over the 72 hours), opening up the possibility that the source of the species responsible for nucleation and/or growth came from these leads. Given the chemical complexity of the marine upper boundary layer compared to near the surface (Zheng et al., 2021), the species involved in particle growth are likely to be different for these two events.

While we have no direct measurements of wind speed at these open leads, measurements performed at the measurement site provide some insights into the potential role of primary sea spray in forming the initial seeds for condensational growth. When wind speeds exceed 4 m s^{-1} over open water, breaking waves tend to produce sea spray aerosol (May et al., 2016; Nilsson et al., 2001). This phenomenon has been previously observed at Utqiagvik in the winter in sub-500 nm particles (Kirpes et al., 2018, 2019). During Event 1, the average wind speed recorded at the site was $5.3 \pm 0.9 \text{ m s}^{-1}$. Lower wind speeds were measured during Event 2 (average of $2.2 \pm 0.2 \text{ m s}^{-1}$) but in both cases there was turbulent ice flow offshore from the measurement site visible in the Barrow sea ice radar (Mahoney & Jones, 2020), which has also been shown to form sea spray aerosol in the Arctic (Nilsson et al., 2001).

Using the SICIMS measurements, we estimated the contribution to the measured growth rate at the measurement site from condensation of H_2SO_4 using the equation provided in Kuang et al. (2010) for Γ , the fraction of growth that can be attributed to H_2SO_4 condensation:

$$\Gamma = \frac{2GR_{meas}}{v_1[\text{H}_2\text{SO}_4]\bar{c}_1} \quad (4)$$

where GR_{meas} is the measured growth rate (nm h^{-1}), $[\text{H}_2\text{SO}_4]$ is the average number concentration of H_2SO_4 measured onsite during the event (molecules cm^{-3}), v_1 is the volume of a hydrated H_2SO_4 molecule ($1.7 \times 10^{-22} \text{ cm}^3$), and \bar{c}_1 is the mean thermal speed of the condensing H_2SO_4 monomer (nm hr^{-1}). From the Γ calculations, the results of which are summarized in Table 1, we estimate that H_2SO_4 condensation accounted for 22% of volumetric growth during Event 1 ($\Gamma = 4.5 \pm 1.5$) and did not contribute substantially to Event 2 ($\Gamma = 139.2 \pm 4.2$). The Γ analysis assumes that the concentration of H_2SO_4 measured during each event represents that which sustained growth during the entire period of growth. It thus assumes that the air mass is exposed to a constant supply of condensing H_2SO_4 and overlooks the role of inhomogeneities during growth (Kivekäs et al., 2016). Nonetheless, the distinct differences in growth rates and apparent influence from H_2SO_4 on observed particle growth are evidence of fundamental differences in the species and circumstances responsible for the observed events. The SSA measured for

bulk aerosol during these events were very similar, suggesting the differences in these events were not impacting larger particle radiative properties.

Table 1. Ultrafine particle growth rates and H₂SO₄ contribution to growth (Γ)

Event	T (°C)	GR _{meas} (nm h ⁻¹)	Γ	[H ₂ SO ₄] (cm ⁻³)
1 (12 March)	-26.4	0.862 ± 0.034	4.5 ± 1.5	3.7 × 10 ⁶
2 (13 – 14 March)	-27.6	2.12 ± 0.07	139.2 ± 4.2	3.0 × 10 ⁵

To further investigate the composition of the particles in each growth event, we next consider the indirect measurements of UFP composition. Figure 6 shows 15 and 35 nm diameter *HGF* data for the two events. An instrument malfunction resulted in missing 15 nm data during Event 1; that issue was resolved midway through Event 2 but as a result we were only able to obtain one reliable measurement of 15 nm *HGF* during that event. Based on the size distribution measurements shown in Figure 4, we postulate that 35 nm particle composition represents both background particles as well as those associated with the growth events. While the condensing species are likely similar for both particle populations, prior studies suggest a higher salt content in larger particles compared to smaller ones if these events began as primary marine aerosol (Prather et al., 2013). Figure 6a shows both the average *HGF* distributions measured during the growth events and the Gaussian fit to each distribution. The sampled particles in both growth events were highly hygroscopic. The *HGF* for 35 nm diameter particles measured during Event 1 was 2.10 ± 0.10. *HGFs* of 15 nm and 35 nm diameter particles during Event 2 were 1.67 and 1.94 ± 0.07, respectively. Measured *HGFs* of 35 nm particles are significantly higher than those measured during the background period (Figure 2c), even compared to the period during 29 March when [H₂SO₄] was similarly high. This difference is evidence of a compositional difference between the particles generated in these two formation events and the background ultrafine particles at the site, and we hypothesize that the former was highly influenced by primary marine particle production whereas the latter is more representative of aged sulfate and organics as discussed above. The 35 nm *HGFs* measured for both events are smaller than those previously reported for 50 nm mobility-selected sea salt particles (*HGF* = 2.3) (Zieger et al., 2017) but fall in the range of nebulized 40 nm sea water proxy with varying amounts of organic material (*HGF* = 1.9 – 2.3, see Figure 2c) (Fuentes et al., 2011) and are larger than that of 35 nm

413 ammonium sulfate ($HGF = 1.65$) (Hämeri et al., 2000). Figure 6b shows that, during Event 1, 35 nm
 414 particle HGF slowly decreased from 2.20 to 1.95. Within measurement uncertainty, the HGF at the end
 415 of Event 1 corresponds to the average HGF measured during Event 2 (1.94 ± 0.07), the latter of which
 416 remained relatively constant throughout its shorter 4-hour period of growth. The HGF distribution of 15
 417 nm particles sampled during Event 2 is narrower than those of 35 nm particles, which indicates that 15
 418 nm particles were compositionally more homogeneous compared to 35 nm particles. The peak HGF for

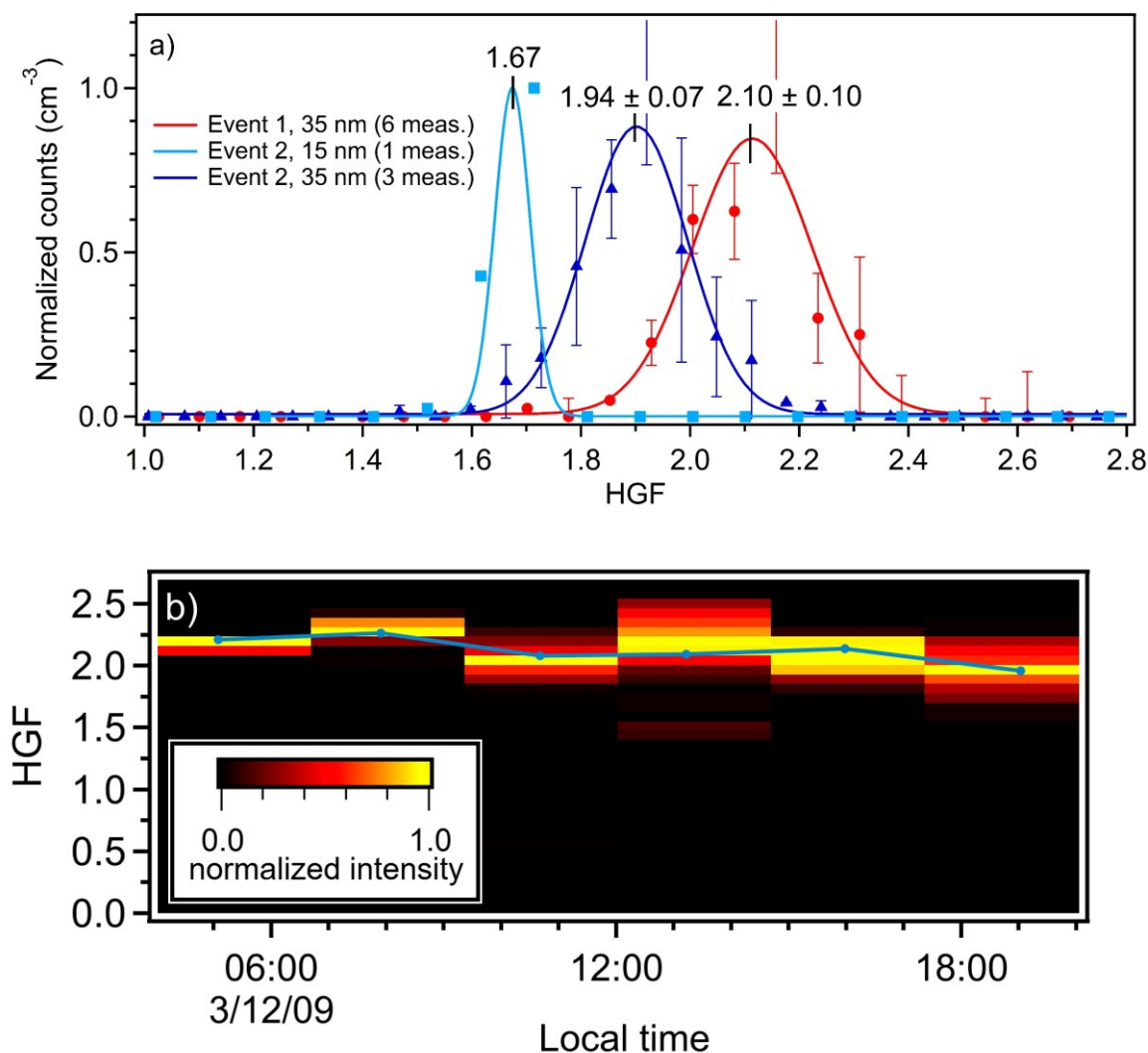


Figure 6. (a) Measured HGF s at 90% RH for 15 and 35 nm size-selected particles during each event (15 nm data missing for Event 1). Markers are the averaged size distributions measured during each event. The error bars represent standard deviation and the number of measurements at each size is shown in the legend. Solid lines are Gaussian fits of the data. Distributions were normalized prior to plotting to facilitate comparison. (b) Time evolution of Event 1 HGF . The Event 2 HGF distribution did not change during the growth period.

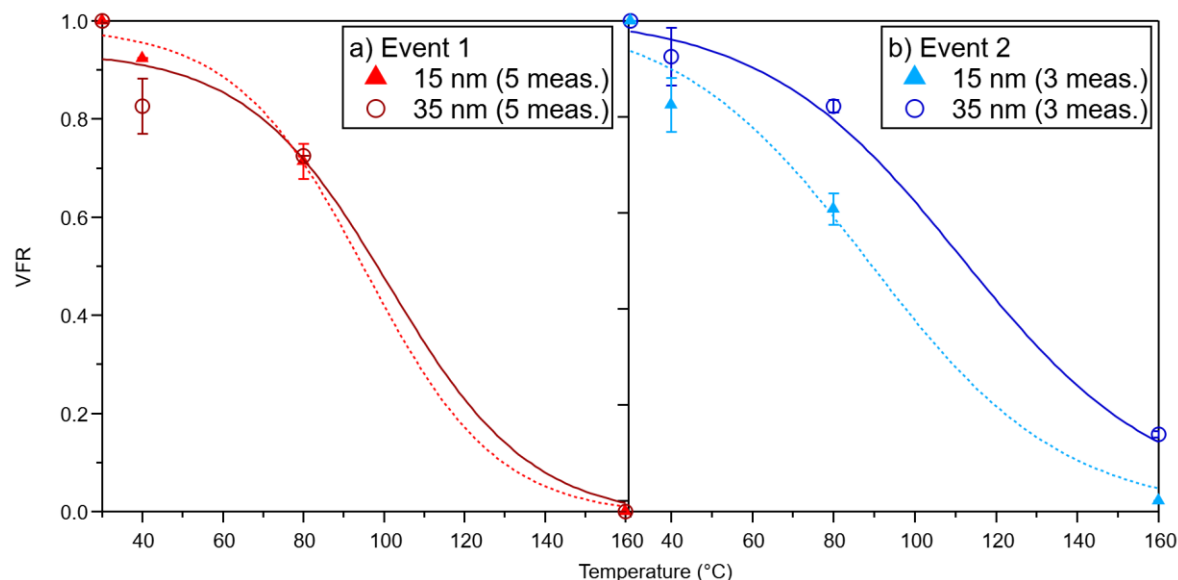


Figure 6. Volume fraction remaining at 40, 80, and 160 °C for 15 and 35 nm size-selected particles during (a) Event 1 and (b) Event 2. The error bars represent standard deviation and the number of measurements at each size is shown in the legend. Initial volume was assumed to be the volume at 30 °C.

15 nm particles, 1.67, is lower than that measured for 35 nm particles, in part due to the Kelvin effect but also likely because of the relatively smaller contribution of primary marine particle seeds to overall particle composition.

Figure 6 shows volatility measurements of 15 and 35 nm mobility-selected particles collected during the events. We note first that the *VFR* data are very similar for both particle sizes measured in Event 1, whereas Event 2 shows more substantial differences between the two sizes. One possible explanation for this can be seen in Figure 4, in which the size distribution of Event 1 (Figure 4a) appears to have a single mode and relatively low concentration of particles larger than 30 nm. In contrast, Event 2 (Figure 4b) occurs with overall higher concentrations of particles larger than 30 nm in diameter. Considering the exceptionally high measured *HGF* measured during both events, it is likely that the differences in *VFR* during Event 2 arise from differences in the relative contributions of primary marine aerosol. In Event 1, 15 nm UFP volume is almost completely lost at 160 °C whereas, in Event 2, 15 nm particles appear to be somewhat less volatile. While generally it is true that background particles show similar volatility at 160 °C (see Figure 3), there is a notable difference in size-dependence of the *VFR* data from these events compared to that of the background period. For the latter, heating to 80 °C resulted in 19.2 ± 0.2 % *VFR* for 35 nm particles, whereas during Event 1, *VFR*s of 71 ± 4 % were measured for 15 nm and 72.57 ± 0.01 % 35 nm diameter particles. Event 2 showed a similar behavior, with *VFR* of 61 ± 3 % for 15 nm particles and 82 ± 1 % for 35 nm particles. Thus, compared to background particles, those

associated with these UFP formation events were significantly less volatile at 80 °C. We attribute this difference in *VFR* at 80 °C to the relative contributions of organics and a low-volatility salt, which in the case of the former is reported as ~40 % for laboratory-generated α -pinene SOA (Huffman et al., 2009) and for the latter as ~100 % for ammonium sulfate and sodium chloride (Huffman et al., 2008; Villani et al., 2007).

To summarize the observations of the two UFP growth events, both events display qualities of regional new particle formation events, specifically sustained and continuous growth that persisted for several hours. This suggests that particles formed over a large region and then were advected over the measurement site, with the first particles detected corresponding to the least aged and the last ones the most aged. Both events are characterized by higher *HGFs* than can be achieved by sulfate salts, and from this we conclude that particles contained significant amounts of highly hygroscopic salts. These salts typically have lower volatility than ammoniated sulfate. The high *HGF* measured are consistent with sea salt consisting of NaCl and other trace elements, which is expected to be non-volatile at 160 °C (Mendes et al., 2016; Villani et al., 2007). The non-volatile nature of NaCl was confirmed for 15 nm particles in laboratory tests with our thermodenuder. Our measurements of 15 and 35 nm *VFR* at 80 °C are consistent with published values for 25 nm *VFR* of marine nanoparticles sampled in Antarctica (Asmi et al., 2010) and observations of 50 nm diameter particle volatility the Arctic and Pacific Oceans (Kim et al., 2015). They are also consistent with reported 30-40 nm particle volatility performed in the North Atlantic (Quinn et al., 2019) and coastal California (Bates et al., 2012), although those observations were performed at higher temperatures (230 °C). Our observations of the importance of a component more hygroscopic than ammonium sulfate in nanoparticle composition is inconsistent with the main conclusions of a study of nanoparticle volatility performed at Svalbard by Giamarelou, et al. (2016), who concluded that ammoniated sulfates dominated 12 nm particle composition. That study, which did not have supporting hygroscopicity measurements nor direct measurements of sulfuric acid, based its conclusion on the observation that ambient particles completely volatilized at 230 °C. The results for Event 2 are consistent with a comprehensive study by Clarke et al., (2006), which concluded that marine UFPs contained a non-volatile core with as much as 90 % by volume of a component that completely volatilized at 300 °C. We hypothesize that the newly formed UFPs observed in this study are comprised of a mixture of volatile organic species and a salt with hygroscopicity similar to sea salt or NaCl, but that largely volatilizes by 160 °C. We are not aware of any aerosol component that has this property but hope that future observations can shed light on this intriguing property of newly formed particles in this region.

Our estimates of volume fraction based on the measured *HGFs* during these events are separated into the composition of 15 nm particles during Event 2, which minimizes potential biases from background particles and is therefore more representative of the species responsible for this event, and that of 35 nm particles during both events, which we hypothesize as being influenced by larger seed particles and higher levels of background particles. For the analysis of 35 nm particle composition, we consider a mixture of sea salt ($HGF = 2.2$), sulfuric acid ($HGF = 1.9$), and oxidized organic ($HGF = 1.2$). We acknowledge that our volatility observations may rule out sea salt but this is the only component that we are aware of that could be responsible for the high *HGFs* observed in this study and so we apply it to this analysis with the caveat that this component has this *HGF* but cannot be pure NaCl. Our Γ analysis (see Table 1) suggests that sulfuric acid may contribute to 22% of particulate volume during Event 1, and we use this information to constrain the contribution by sulfuric acid to composition during that event. For the analysis of 15 nm particle composition during Event 2, we use the following *HGFs* from prior studies: sea salt ($HGF = 2.0$) (Zieger et al., 2017) and oxidized organic ($HGF = 1.1$) (Virkkula et al., 1999). Table 2 summarizes the results of the analysis of these *HGF* measurements by the ZSR method. During both Events 1 and 2, 35 nm diameter particles contained significant amounts of the very hygroscopic “sea salt”, with an estimated volume fraction (ϵ_{SS}) of 0.74. The balance of composition is predominantly sulfuric acid for Event 1 ($\epsilon_{SA} = 0.22$), and oxidized organic for Event 2 ($\epsilon_{ORG} = 0.26$). Oxidized organics contributed a small amount to 35 nm particle composition in Event 1 ($\epsilon_{ORG} = 0.04$). Even though these results are based on measured *HGF*, they are qualitatively in agreement with the measurements of volatility if it were true that the oxidized organics were of low volatility. This possibility is also suggested in the study of Arctic aerosol volatility by Giamarelou et al. (2016). Finally, the significant contribution of “sea salt” to 35 nm particle composition in both events agrees qualitatively with the analyses of the size distribution, back trajectories and wind data, all of which point to the likelihood that marine emissions were responsible for the initiation of these events. As for the 15 nm diameter particles most associated with the UFP growth event, our analysis suggests that this event may have also begun with the formation of primary hygroscopic sea salt-like particles, and then subsequently

Table 2. Estimates of the volume fraction of representative compound classes during UFP formation events, based on analysis of *HGF* data using the ZSR mixing rule. ϵ_{SS} : volume fraction of hygroscopic sea salt, ϵ_{SA} : volume fraction of sulfuric acid, ϵ_{ORG} : volume fraction of organic compounds.

Event	Dp (nm)	ϵ_{SS}	ϵ_{SA}	ϵ_{ORG}
1 (12 March)	35	0.74	0.22	0.04
2 (13 – 14 March)	15	0.63	0	0.37
	35	0.74	0	0.26

grew from the condensation of organic compounds. As mentioned previously, Event 2 was first observed at the site with a measured modal diameter of 7 nm, so while this qualitatively agrees with the *HGF* measurements that suggest a sea salt-like core, the *HGF* measurements suggest a much higher volume fraction.

4 Conclusion

In this manuscript, we report indirect composition measurements of ultrafine particles in Utqiagvik, Alaska, observed during late winter and early spring (5 March – 14 April 2009). Our estimates of size-resolved particle composition combine measurements of particle hygroscopicity and volatility with those of gas-phase H_2SO_4 . During “background” periods with minimal local anthropogenic influence, ultrafine particles in this region were characterized by low concentrations, especially sub-20 nm diameter particles. Under these conditions, particles exhibited moderate hygroscopic growth that suggests a mixed organic-inorganic composition. Volatility measurements support this observation, with less than 20% *VFR* measured for sub-100 nm particles. We estimated the volume fractions of representative compounds using the ZSR method and found that ammoniated sulfate (~30% by volume) and low-hygroscopicity oxidized organics (~70% by volume) could account for the measured hygroscopicity of 35 nm particles. Gas-phase H_2SO_4 generally trends with solar radiation but did not follow a regular diurnal pattern in this campaign. We also analyzed two ultrafine particle growth events wherein the properties of the particles differed greatly from those measured during the background period. Both growth events produced highly hygroscopic particles, but the differences in the average measured hygroscopic growth factors (Event 1: 2.1; Event 2: 1.9), as well as growth rates and H_2SO_4 contributions to growth, suggest differences in their chemical composition. HYSPLIT back trajectories and MODIS satellite imagery suggest that Event 1 was likely influenced by upper marine boundary layer processes, while Event 2 passed over open leads in the lower boundary layer. Both hygroscopicity and volatility data show that particles in both growth events contain a significant volume fraction of high hygroscopicity, low volatility species and support a role for primary marine emissions similar to sea salt as the initial seed for these events. The preponderance of evidence suggests that Event 1 particles were composed of mixtures of sea salt-like species and sulfuric acid, whereas Event 2 particles contained similar levels of salt but the balance of the composition was oxidized organics. This sea salt-like species, which is highly hygroscopic but more volatile than NaCl, is not known and illustrates the necessity of further measurements in this region. This study illuminates the importance of a multi-pronged approach to indirect measurements of ultrafine particle composition and illustrates the variability that exists between background aerosol and newly formed aerosol. It also highlights to potentially important role of low-

volatility, high-hygroscopicity primary marine species like sea salt as initiators of ultrafine particle production in the Arctic late-winter. Additional measurements during this understudied time of year should be performed to better elucidate the processes driving particle production in this important region.

Acknowledgement

The authors wish to thank the organizers of the OASIS 2009 field campaign, the Barrow Arctic Science Consortium for logistics support, and all of the researchers who contributed to the campaign. The authors gratefully acknowledge funding for the analysis of this dataset by the Department of Energy, grant DE-SC0019000. All data from the OASIS Barrow 2009 field campaign are publicly available at [10.5065/D6CJ8BM3](https://doi.org/10.5065/D6CJ8BM3).

Citations

- Abbatt, J. P. D., Leaitch, W. R., Aliabadi, A. A., Bertram, A. K., Blanchet, J.-P., Boivin-Rioux, A., et al. (2019). Overview paper: New insights into aerosol and climate in the Arctic. *Atmospheric Chemistry and Physics*, 19. <https://doi.org/10.5194/acp-19-2527-2019>
- Allan, J. D., Williams, P. I., Najera, J., Whitehead, J. D., Flynn, M. J., Taylor, J. W., et al. (2015). Iodine observed in new particle formation events in the Arctic atmosphere during ACCACIA. *Atmospheric Chemistry and Physics*, 15(10), 5599–5609. <https://doi.org/10.5194/acp-15-5599-2015>
- Asmi, E., Frey, A., Virkkula, A., Ehn, M., Manninen, H. E., Timonen, H., et al. (2010). Hygroscopicity and chemical composition of Antarctic sub-micrometre aerosol particles and observations of new particle formation. *Atmospheric Chemistry and Physics*, 10, 4253–4271. <https://doi.org/10.5194/acp-10-4253-2010>
- Asmi, E., Kondratyev, V., Brus, D., Laurila, T., Lihavainen, H., Backman, J., et al. (2016). Aerosol size distribution seasonal characteristics measured in Tiksi, Russian Arctic. *Atmospheric Chemistry and Physics*, 16(3), 1271–1287. <https://doi.org/10.5194/acp-16-1271-2016>
- Baccarini, A., Karlsson, L., Dommen, J., Duplessis, P., Vüllers, J., Brooks, I. M., et al. (2020). Frequent new particle formation over the high Arctic pack ice by enhanced iodine emissions. *Nature Communications*, 11(1). <https://doi.org/10.1038/s41467-020-18551-0>
- Barrie, L. A. (1986). Arctic air pollution: An overview of current knowledge. *Atmospheric Environment*, 20(4), 643–663. [https://doi.org/10.1016/0004-6981\(86\)90180-0](https://doi.org/10.1016/0004-6981(86)90180-0)
- Bates, T. S., Quinn, P. K., Frossard, A. A., Russell, L. M., Hakala, J., Petäjä, T., et al. (2012). Measurements of ocean derived aerosol off the coast of California. *Journal of Geophysical Research Atmospheres*, 117(12), 0–15. <https://doi.org/10.1029/2012JD017588>
- Bergin, M. H., Ogren, J. A., Schwartz, S. E., & McInnes, L. M. (1997). Evaporation of ammonium nitrate aerosol in a heated nephelometer: Implications for field measurements. *Environmental Science and Technology*, 31(10), 2878–2883. <https://doi.org/10.1021/es970089h>
- Bodhaine, B. A., Harris, J. M., & Herbert, G. A. (1981). Aerosol light scattering and condensation nuclei measurements at Barrow, Alaska. *Atmospheric Environment*, 15(8), 1375–1389.

567 [https://doi.org/10.1016/0004-6981\(81\)90344-9](https://doi.org/10.1016/0004-6981(81)90344-9)

568 Boylan, P., Helmig, D., Staebler, R., Turnipseed, A., Fairall, C., & Neff, W. (2014). Boundary layer
569 dynamics during the Ocean-Atmosphere-Sea-Ice-Snow (OASIS) 2009 experiment at Barrow, AK.
570 *Journal of Geophysical Research: Atmospheres*, 119(5), 2261–2278.
571 <https://doi.org/10.1002/2013JD020299>

572 Browse, J., Carslaw, K. S., Arnold, S. R., Pringle, K., & Boucher, O. (2012). The scavenging processes
573 controlling the seasonal cycle in Arctic sulphate and black carbon aerosol. *Atmospheric Chemistry*
574 *and Physics*, 12(15), 6775–6798. <https://doi.org/10.5194/acp-12-6775-2012>

575 Burkart, J., Hodshire, A. L., Mungall, E. L., Pierce, J. R., Collins, D. B., Ladino, L. A., et al. (2017).
576 Organic Condensation and Particle Growth to CCN Sizes in the Summertime Marine Arctic Is
577 Driven by Materials More Semivolatile Than at Continental Sites. *Geophysical Research Letters*,
578 44(20), 10,725–10,734. <https://doi.org/10.1002/2017GL075671>

579 Burtscher, H., Baltensperger, U., Bukowiecki, N., Cohn, P., Hüglin, C., Mohr, M., et al. (2001).
580 Separation of volatile and non-volatile aerosol fractions by thermodesorption: Instrumental
581 development and applications. *Journal of Aerosol Science*, 32(4), 427–442.
582 [https://doi.org/10.1016/S0021-8502\(00\)00089-6](https://doi.org/10.1016/S0021-8502(00)00089-6)

583 Chang, R. Y. W., Sjostedt, S. J., Pierce, J. R., Papakyriakou, T. N., Scarratt, M. G., Michaud, S., et al.
584 (2011). Relating atmospheric and oceanic DMS levels to particle nucleation events in the Canadian
585 Arctic. *Journal of Geophysical Research Atmospheres*, 116(21).
586 <https://doi.org/10.1029/2011JD015926>

587 Clarke, A. D., Charlson, R. J., & Radke, L. F. (1984). Airborne observations of Arctic aerosol, IV:
588 Optical properties of Arctic haze. *Geophysical Research Letters*, 11(5).
589 <https://doi.org/10.1029/GL011i005p00405>

590 Clarke, A. D., Owens, S. R., & Zhou, J. (2006). An ultrafine sea-salt flux from breaking waves:
591 Implications for cloud condensation nuclei in the remote marine atmosphere. *Journal of*
592 *Geophysical Research*, 111(D6), D06202. <https://doi.org/10.1029/2005JD006565>

593 Cochran, R. E., Ryder, O. S., Grassian, V. H., & Prather, K. A. (2017). Sea spray aerosol: The chemical
594 link between the oceans, atmosphere, and climate. *Accounts of Chemical Research*. American
595 Chemical Society. <https://doi.org/10.1021/acs.accounts.6b00603>

596 Collins, D. B., Burkart, J., Y-W Chang, R., Lizotte, M., Boivin-Rioux, A., Blais, M., et al. (2017).
597 Frequent ultrafine particle formation and growth in Canadian Arctic marine and coastal
598 environments. *Atmospheric Chemistry and Physics*, 17, 13119–13138. <https://doi.org/10.5194/acp-17-13119-2017>

600 Covert, D. S., & Heintzenberg, J. (1993). Size distributions and chemical properties of aerosol at Ny
601 Ålesund, Svalbard. *Atmospheric Environment Part A, General Topics*, 27(17–18), 2989–2997.
602 [https://doi.org/10.1016/0960-1686\(93\)90331-R](https://doi.org/10.1016/0960-1686(93)90331-R)

603 Croft, B., Martin, R. V., Leaitch, W. R., Tunved, P., Breider, T. J., D’Andrea, S. D., & Pierce, J. R.
604 (2016). Processes controlling the annual cycle of Arctic aerosol number and size distributions.
605 *Atmospheric Chemistry and Physics*, 16, 3665–3682. <https://doi.org/10.5194/acp-16-3665-2016>

606 Croft, B., Martin, R. V., Richard Leaitch, W., Burkart, J., Y-W Chang, R., Collins, D. B., et al. (2019).
607 Arctic marine secondary organic aerosol contributes significantly to summertime particle size
608 distributions in the Canadian Arctic Archipelago. *Atmospheric Chemistry and Physics*, 19, 2787–
609 2812. <https://doi.org/10.5194/acp-19-2787-2019>

610 Dal Maso, M., Kulmala, M., Riipinen, I., Wagner, R., Hussein, T., Aalto, P. P., & Lehtinen, K. E. J.
611 (2005). Formation and growth of fresh atmospheric aerosols: Eight years of aerosol size distribution
612 data from SMEAR II, Hyytiälä, Finland. *Boreal Environment Research*, 10(5), 323–336.

613 Dall'Osto, M., Beddows, D. C. S., Tunved, P., Krejci, R., Ström, J., Hansson, H. C., et al. (2017). Arctic
614 sea ice melt leads to atmospheric new particle formation. *Scientific Reports*, 7(1), 1–10.
615 <https://doi.org/10.1038/s41598-017-03328-1>

616 Dall'Osto, M., Simo, R., Harrison, R. M., Beddows, D. C. S., Saiz-Lopez, A., Lange, R., et al. (2018).
617 Abiotic and biotic sources influencing spring new particle formation in North East Greenland.
618 *Atmospheric Environment*, 190, 126–134. <https://doi.org/10.1016/j.atmosenv.2018.07.019>

619 Dall'Osto, M., Geels, C., Beddows, D. C. S., Boertmann, D., Lange, R., Nøjgaard, J. K., et al. (2018).
620 Regions of open water and melting sea ice drive new particle formation in North East Greenland.
621 *Scientific Reports*, 8(1), 1–10. <https://doi.org/10.1038/s41598-018-24426-8>

622 Ferek, R. J., Hobbs, P. V., Radke, L. F., Herring, J. A., Sturges, W. T., & Cota, G. F. (1995). Dimethyl
623 sulfide in the Arctic atmosphere. *Journal of Geophysical Research*, 100(D12), 26093–26104.
624 <https://doi.org/10.1029/95jd02374>

625 Flowers, B. A., Dubey, M. K., Mazzoleni, C., Stone, E. A., Schauer, J. J., Kim, S. W., & Yoon, S. C.
626 (2010). Optical-chemical-microphysical relationships and closure studies for mixed carbonaceous
627 aerosols observed at Jeju Island; 3-laser photoacoustic spectrometer, particle sizing, and filter
628 analysis. *Atmospheric Chemistry and Physics*, 10(21), 10387–10398. [https://doi.org/10.5194/acp-10-](https://doi.org/10.5194/acp-10-10387-2010)
629 [10387-2010](https://doi.org/10.5194/acp-10-10387-2010)

630 Frieß, U., Sihler, H., Sander, R., Phler, D., Yilmaz, S., & Platt, U. (2011). The vertical distribution of BrO
631 and aerosols in the Arctic: Measurements by active and passive differential optical absorption
632 spectroscopy. *Journal of Geophysical Research Atmospheres*, 116(18).
633 <https://doi.org/10.1029/2011JD015938>

634 Frossard, A. A., Shaw, P. M., Russell, L. M., Kroll, J. H., Canagaratna, M. R., Worsnop, D. R., et al.
635 (2011). Springtime Arctic haze contributions of submicron organic particles from European and
636 Asian combustion sources. *Journal of Geophysical Research-Atmospheres*, 116.
637 <https://doi.org/10.1029/2010jd015178>

638 Frossard, A. A., Russell, L. M., Massoli, P., Bates, T. S., & Quinn, P. K. (2014). Side-by-side comparison
639 of four techniques explains the apparent differences in the organic composition of generated and
640 ambient marine aerosol particles. *Aerosol Science and Technology*, 48(3), v–x.
641 <https://doi.org/10.1080/02786826.2013.879979>

642 Fuentes, E., Coe, H., Green, D., & McFiggans, G. (2011). On the impacts of phytoplankton-derived
643 organic matter on the properties of the primary marine aerosol - Part 2: Composition, hygroscopicity
644 and cloud condensation activity. *Atmospheric Chemistry and Physics*, 11(6), 2585–2602.
645 <https://doi.org/10.5194/acp-11-2585-2011>

646 Garrett, T. J., Brattström, S., Sharma, S., Worthy, D. E. J., & Novelli, P. (2011). The role of scavenging in
647 the seasonal transport of black carbon and sulfate to the Arctic. *Geophysical Research Letters*,
648 38(16). <https://doi.org/10.1029/2011GL048221>

649 Ghahremaninezhad, R., Norman, A.-L., Abbatt, J. P. D., Levasseur, M., & Thomas, J. L. (2016).
650 Biogenic, anthropogenic and sea salt sulfate size-segregated aerosols in the Arctic summer.
651 *Atmospheric Chemistry and Physics*, 16(8), 5191–5202. <https://doi.org/10.5194/acp-16-5191-2016>

652 Giamarelou, M., Eleftheriadis, K., Nyeki, S., Tunved, P., Torseth, K., & Biskos, G. (2016). Indirect

653 evidence of the composition of nucleation mode atmospheric particles in the high Arctic. *Journal of*
654 *Geophysical Research: Atmospheres*, 121(2), 965–975. <https://doi.org/10.1002/2015JD023646>

655 Gysel, M., Weingartner, E., Nyeki, S., Paulsen, D., Baltensperger, U., Galambos, I., & Kiss, G. (2004).
656 Hygroscopic properties of water-soluble matter and humic-like organics in atmospheric fine aerosol.
657 *Atmospheric Chemistry and Physics*, 4(1), 35–50. <https://doi.org/10.5194/acp-4-35-2004>

658 Gysel, M., McFiggans, G. B., & Coe, H. (2009). Inversion of tandem differential mobility analyser
659 (TDMA) measurements. *Journal of Aerosol Science*, 40(2).
660 <https://doi.org/10.1016/j.jaerosci.2008.07.013>

661 Häkkinen, S. A. K., Äijälä, M., Lehtipalo, K., Junninen, H., Backman, J., Virkkula, A., et al. (2012).
662 Long-term volatility measurements of submicron atmospheric aerosol in Hyytiälä, Finland.
663 *Atmospheric Chemistry and Physics*, 12(22), 10771–10786. [https://doi.org/10.5194/acp-12-10771-](https://doi.org/10.5194/acp-12-10771-2012)
664 2012

665 Hall, D. K., & Riggs, G. A. (2015). MODIS/Aqua Sea Ice Extent 5-Min L2 Swath 1km, Version 6
666 [March 2009]. Retrieved February 18, 2021, from <https://doi.org/10.5067/MODIS/MYD29.006>

667 Hämeri, K., Väkevä, M., Hansson, H.-C., & Laaksonen, A. (2000). Hygroscopic growth of ultrafine
668 ammonium sulphate aerosol measured using an ultrafine tandem differential mobility analyzer.
669 *Journal of Geophysical Research: Atmospheres*, 105(D17), 22231–22242.
670 <https://doi.org/10.1029/2000JD900220>

671 Hawkins, L. N., & Russell, L. M. (2010). Polysaccharides, Proteins, and Phytoplankton Fragments: Four
672 Chemically Distinct Types of Marine Primary Organic Aerosol Classified by Single Particle
673 Spectromicroscopy. *Advances in Meteorology*, 2010, 1–14. <https://doi.org/10.1155/2010/612132>

674 Heintzenberg, J. (1982). Size-segregated measurements of particulate elemental carbon and aerosol light
675 absorption at remote arctic locations. *Atmospheric Environment (1967)*, 16(10), 2461–2469.
676 [https://doi.org/10.1016/0004-6981\(82\)90136-6](https://doi.org/10.1016/0004-6981(82)90136-6)

677 Heintzenberg, J., Leck, C., & Tunved, P. (2015). Potential source regions and processes of aerosol in the
678 summer Arctic. *Atmospheric Chemistry and Physics*, 15, 6487–6502. [https://doi.org/10.5194/acp-](https://doi.org/10.5194/acp-15-6487-2015)
679 15-6487-2015

680 Hinds, William C. (1999). *Aerosol Technology: Properties, Behavior, and Measurement of Airborne*
681 *Particles*, 2nd Edition | Wiley. Retrieved May 17, 2021, from [https://www.wiley.com/en-](https://www.wiley.com/en-us/Aerosol+Technology%3A+Properties%2C+Behavior%2C+and+Measurement+of+Airborne+Particles%2C+2nd+Edition-p-9780471194101)
682 [us/Aerosol+Technology%3A+Properties%2C+Behavior%2C+and+Measurement+of+Airborne+Part](https://www.wiley.com/en-us/Aerosol+Technology%3A+Properties%2C+Behavior%2C+and+Measurement+of+Airborne+Particles%2C+2nd+Edition-p-9780471194101)
683 [icles%2C+2nd+Edition-p-9780471194101](https://www.wiley.com/en-us/Aerosol+Technology%3A+Properties%2C+Behavior%2C+and+Measurement+of+Airborne+Particles%2C+2nd+Edition-p-9780471194101)

684 Huffman, J. A., Ziemann, P. J., Jayne, J. T., Worsnop, D. R., & Jimenez, J. L. (2008). Development and
685 Characterization of a Fast-Stepping/Scanning Thermodenuder for Chemically-Resolved Aerosol
686 Volatility Measurements. *Aerosol Science and Technology*, 42(5), 395–407.
687 <https://doi.org/10.1080/02786820802104981>

688 Huffman, J. A., Docherty, K. S., Mohr, C., Cubison, M. J., Ulbrich, I. M., Ziemann, P. J., et al. (2009).
689 Chemically-resolved volatility measurements of organic aerosol from different sources.
690 *Environmental Science and Technology*, 43(14), 5351–5357. <https://doi.org/10.1021/es803539d>

691 Jennings, S. G., O'Dowd, C. D., Cooke, W. F., Sheridan, P. J., & Cachier, H. (1994). Volatility of
692 elemental carbon. *Geophysical Research Letters*, 21(16), 1719–1722.
693 <https://doi.org/10.1029/94GL01423>

694 Karl, M., Leck, C., Gross, A., & Pirjola, L. (2012). A study of new particle formation in the marine
695 boundary layer over the central Arctic Ocean using a flexible multicomponent aerosol dynamic

696 model. *Tellus B: Chemical and Physical Meteorology*, 64(1).
 697 <https://doi.org/10.3402/tellusb.v64i0.17158>

698 Karl, M., Leck, C., Coz, E., & Heintzenberg, J. (2013). Marine nanogels as a source of atmospheric
 699 nanoparticles in the high Arctic. *Geophysical Research Letters*, 40(14), 3738–3743.
 700 <https://doi.org/10.1002/grl.50661>

701 Kecorius, S., Vogl, T., Paasonen, P., Lampilahti, J., Rothenberg, D., Wex, H., et al. (2019). New particle
 702 formation and its effect on cloud condensation nuclei abundance in the summer Arctic: a case study
 703 in the Fram Strait and Barents Sea. *Atmospheric Chemistry and Physics*, 19(22), 14339–14364.
 704 <https://doi.org/10.5194/acp-19-14339-2019>

705 Keith, C. H., & Arons, A. B. (1954). The Growth of Sea-Salt Particles by Condensation of Atmospheric
 706 Water Vapor. *Journal of Meteorology*, 11(3). [https://doi.org/10.1175/1520-0469\(1954\)011<0173:TGOSSP>2.0.CO;2](https://doi.org/10.1175/1520-0469(1954)011<0173:TGOSSP>2.0.CO;2)

707
 708 Kim, G., Cho, H., Seo, A., Kim, D., Gim, Y., Yong Lee, B., et al. (2015). Comparison of Hygroscopicity,
 709 Volatility, and Mixing State of Submicrometer Particles between Cruises over the Arctic Ocean and
 710 the Pacific Ocean. *Environmental Science and Technology*, 49, 51.
 711 <https://doi.org/10.1021/acs.est.5b01505>

712 Kirpes, R. M., Bondy, A. L., Bonanno, D., Moffet, R. C., Wang, B., Laskin, A., et al. (2018). Secondary
 713 sulfate is internally mixed with sea spray aerosol and organic aerosol in the winter Arctic.
 714 *Atmospheric Chemistry and Physics*, 18(6), 3937–3949. <https://doi.org/10.5194/acp-18-3937-2018>

715 Kirpes, R. M., Bonanno, D., May, N. W., Fraund, M., Barget, A. J., Moffet, R. C., et al. (2019a).
 716 Wintertime Arctic Sea Spray Aerosol Composition Controlled by Sea Ice Lead Microbiology. *ACS*
 717 *Central Science*, 5(11), 1760–1767. <https://doi.org/10.1021/acscentsci.9b00541>

718 Kirpes, R. M., Bonanno, D., May, N. W., Fraund, M., Barget, A. J., Moffet, R. C., et al. (2019b).
 719 Wintertime Arctic Sea Spray Aerosol Composition Controlled by Sea Ice Lead Microbiology. *ACS*
 720 *Central Science*, 5(11), 1760–1767. <https://doi.org/10.1021/acscentsci.9b00541>

721 Kivekäs, N., Carpmann, J., Roldin, P., Leppä, J., O'Connor, E., Kristensson, A., & Asmi, E. (2016).
 722 Coupling an aerosol box model with one-dimensional flow: a tool for understanding observations of
 723 new particle formation events. *Tellus B: Chemical and Physical Meteorology*, 68(1), 29706.
 724 <https://doi.org/10.3402/tellusb.v68.29706>

725 Kolesar, K. R., Cellini, J., Peterson, P. K., Jefferson, A., Tuch, T., Birmili, W., et al. (2017). Effect of
 726 Prudhoe Bay emissions on atmospheric aerosol growth events observed in Utqiagvik (Barrow),
 727 Alaska. *Atmospheric Environment*, 152, 146–155. <https://doi.org/10.1016/j.atmosenv.2016.12.019>

728 Kreidenweis, S. M., McInnes, L. M., & Brechtel, F. J. (1998). Observations of aerosol volatility and
 729 elemental composition at Macquarie Island during the First Aerosol Characterization Experiment
 730 (ACE 1). *Journal of Geophysical Research: Atmospheres*, 103(D13), 16511–16524.
 731 <https://doi.org/10.1029/98JD00800>

732 Kuang, C., Riipinen, I., Sihto, S.-L., Kulmala, M., McCormick, A. V., & McMurry, P. H. (2010). An
 733 improved criterion for new particle formation in diverse atmospheric environments. *Atmospheric*
 734 *Chemistry and Physics*, 10(17), 8469–8480. <https://doi.org/10.5194/acp-10-8469-2010>

735 Kupiszewski, P., Leck, C., Tjernström, M., Sjogren, S., Sedlar, J., Graus, M., et al. (2013). Vertical
 736 profiling of aerosol particles and trace gases over the central Arctic Ocean during summer.
 737 *Atmospheric Chemistry and Physics*, 13(24), 12405–12431. <https://doi.org/10.5194/acp-13-12405-2013>

738

739 Lance, S., Raatikainen, T., Onasch, T. B., Worsnop, D. R., Yu, X. Y., Alexander, M. L., et al. (2013).
 740 Aerosol mixing state, hygroscopic growth and cloud activation efficiency during MIRAGE 2006.
 741 *Atmospheric Chemistry and Physics*, 13(9), 5049–5062. <https://doi.org/10.5194/acp-13-5049-2013>
 742 Law, K. S., & Stohl, A. (2007, March 16). Arctic air pollution: Origins and impacts. *Science*. American
 743 Association for the Advancement of Science. <https://doi.org/10.1126/science.1137695>
 744 Leaitch, W. R., Sharma, S., Huang, L., Toom-Sauntry, D., Chivulescu, A., Macdonald, A. M., et al.
 745 (2013). Dimethyl sulfide control of the clean summertime Arctic aerosol and cloud. *Elementa:*
 746 *Science of the Anthropocene*, 1(0), 000017. <https://doi.org/10.12952/journal.elementa.000017>
 747 Leck, C., Gao, Q., Mashayekhy Rad, F., & Nilsson, U. (2013). Atmospheric Chemistry and Physics Size-
 748 resolved atmospheric particulate polysaccharides in the high summer Arctic. *Atmospheric Chemistry*
 749 *and Physics*, 13, 12573–12588. <https://doi.org/10.5194/acp-13-12573-2013>
 750 Leck, Caroline, & Bigg, E. K. (2010). New Particle Formation of Marine Biological Origin. *Aerosol*
 751 *Science and Technology*, 44(7), 570–577. <https://doi.org/10.1080/02786826.2010.481222>
 752 Liao, J., Huey, L. G., Tanner, D. J., Flocke, F. M., Orlando, J. J., Neuman, J. A., et al. (2012).
 753 Observations of inorganic bromine (HOBr, BrO, and Br₂) speciation at Barrow, Alaska, in spring
 754 2009. *Journal of Geophysical Research: Atmospheres*, 117(D14).
 755 [https://doi.org/10.1029/2011JD016641@10.1002/\(ISSN\)2169-8996.OASIS1](https://doi.org/10.1029/2011JD016641@10.1002/(ISSN)2169-8996.OASIS1)
 756 Malm, W. C., & Kreidenweis, S. M. (1997). The effects of models of aerosol hygroscopicity on the
 757 apportionment of extinction. *Atmospheric Environment*, 31(13), 1965–1976.
 758 [https://doi.org/10.1016/S1352-2310\(96\)00355-X](https://doi.org/10.1016/S1352-2310(96)00355-X)
 759 Mauldin, R. L., Frost, G. J., Chen, G., Tanner, D. J., Prevot, A. S. H., Davis, D. D., & Eisele, F. L.
 760 (1998). OH measurements during the First Aerosol Characterization Experiment (ACE 1):
 761 Observations and model comparisons. *Journal of Geophysical Research: Atmospheres*, 103(D13),
 762 16713–16729. <https://doi.org/10.1029/98JD00882>
 763 May, N. W., Quinn, P. K., McNamara, S. M., & Pratt, K. A. (2016). Multiyear study of the dependence of
 764 sea salt aerosol on wind speed and sea ice conditions in the coastal Arctic. *Journal of Geophysical*
 765 *Research: Atmospheres*, 121(15), 9208–9219. <https://doi.org/10.1002/2016JD025273>
 766 Mendes, L., Eleftheriadis, K., & Biskos, G. (2016). Performance comparison of two thermodenuders in
 767 Volatility Tandem DMA measurements. *Journal of Aerosol Science*, 92, 38–52.
 768 <https://doi.org/10.1016/j.jaerosci.2015.10.002>
 769 NCAR. (2012). Location information and pictures of the OASIS Barrow field intensive Spring 2009.
 770 Retrieved February 3, 2021, from <https://data.eol.ucar.edu/dataset/106.366>
 771 Nguyen, Q. T., Glasius, M., Sørensen, L. L., Jensen, B., Skov, H., Birmili, W., et al. (2016). Seasonal
 772 variation of atmospheric particle number concentrations, new particle formation and atmospheric
 773 oxidation capacity at the high Arctic site Villum Research Station, Station Nord. *Atmospheric*
 774 *Chemistry and Physics*, 16, 11319–11336. <https://doi.org/10.5194/acp-16-11319-2016>
 775 Nilsson, E. D., Rannik, Ü., Swietlicki, E., Leck, C., Aalto, P. P., Zhou, J., & Norman, M. (2001).
 776 Turbulent aerosol fluxes over the Arctic Ocean: 2. Wind-driven sources from the sea. *Journal of*
 777 *Geophysical Research: Atmospheres*, 106(D23), 32139–32154.
 778 <https://doi.org/10.1029/2000JD900747>
 779 Nyeki, S., Coulson, G., Colbeck, I., Eleftheriadis, K., Baltensperger, U., & Beine, H. J. (2005). Overview
 780 of aerosol microphysics at Arctic sunrise: measurements during the NICE renoxification study.
 781 *Tellus B*, 57(1), 40–50. <https://doi.org/10.1111/j.1600-0889.2005.00122.x>

782 O'Dowd, C. D., Facchini, M. C., Cavalli, F., Ceburnis, D., Mircea, M., Decesari, S., et al. (2004).
783 Biogenically driven organic contribution to marine aerosol. *Nature*, 431(7009), 676–680.
784 <https://doi.org/10.1038/nature02959>

785 Ovadnevaite, J., Ceburnis, D., Martucci, G., Bialek, J., Monahan, C., Rinaldi, M., et al. (2011). Primary
786 marine organic aerosol: A dichotomy of low hygroscopicity and high CCN activity. *Geophysical*
787 *Research Letters*, 38(21). <https://doi.org/https://doi.org/10.1029/2011GL048869>

788 Patterson, E. M., Marshall, B. T., & Rahn, K. A. (1967). Radiative properties of the arctic aerosol.
789 *Atmospheric Environment*, 16(12), 2967–2977. [https://doi.org/10.1016/0004-6981\(82\)90048-8](https://doi.org/10.1016/0004-6981(82)90048-8)

790 Polissar, A. V., Hopke, P. K., & Harris, J. M. (2001). Source regions for atmospheric aerosol measured at
791 Barrow, Alaska. *Environmental Science and Technology*, 35(21), 4214–4226.
792 <https://doi.org/10.1021/es0107529>

793 Prather, K. A., Bertram, T. H., Grassian, V. H., Deane, G. B., Stokes, M. D., DeMott, P. J., et al. (2013).
794 Bringing the ocean into the laboratory to probe the chemical complexity of sea spray aerosol.
795 *Proceedings of the National Academy of Sciences of the United States of America*, 110(19), 7550–
796 7555. <https://doi.org/10.1073/pnas.1300262110>

797 Quinn, P. K., Miller, T. L., Bates, T. S., Ogren, J. A., Andrews, E., & Shaw, G. E. (2002). A 3-year
798 record of simultaneously measured aerosol chemical and optical properties at Barrow, Alaska.
799 *Journal of Geophysical Research D: Atmospheres*, 107(11), AAC 8-1.
800 <https://doi.org/10.1029/2001jd001248>

801 Quinn, P. K., Shaw, G., Andrews, E., & Dutton, E. G. (2007). Arctic haze: current trends and knowledge
802 gaps. *Tellus B: Chemical and Physical Meteorology*. [https://doi.org/10.1111/j.1600-](https://doi.org/10.1111/j.1600-0889.2006.00236.x)
803 [0889.2006.00236.x](https://doi.org/10.1111/j.1600-0889.2006.00236.x)

804 Quinn, P. K., Bates, T. S., Schulz, K., & Shaw, G. E. (2009). Decadal trends in aerosol chemical
805 composition at Barrow, Alaska: 1976–2008. *Atmospheric Chemistry and Physics*, 9, 8883–8888.
806 Retrieved from www.atmos-chem-phys.net/9/8883/2009/

807 Quinn, P. K., Bates, T. S., Coffman, D. J., Upchurch, L., Johnson, J. E., Moore, R., et al. (2019). Seasonal
808 Variations in Western North Atlantic Remote Marine Aerosol Properties. *Journal of Geophysical*
809 *Research: Atmospheres*, 124(24), 14240–14261. <https://doi.org/10.1029/2019JD031740>

810 Rahn, K. A. (1981). Relative importances of North America and Eurasia as sources of arctic aerosol.
811 *Atmospheric Environment* (1967), 15(8), 1447–1455. [https://doi.org/10.1016/0004-6981\(81\)90351-6](https://doi.org/10.1016/0004-6981(81)90351-6)

812 Rolph, G., Stein, A., & Stunder, B. (2017). Real-time Environmental Applications and Display sYstem:
813 READY. *Environmental Modelling & Software*, 95(1364–8152), 210–228. Retrieved from
814 <https://doi.org/10.1016/j.envsoft.2017.06.025>

815 Sjogren, S., Gysel, M., Weingartner, E., Baltensperger, U., Cubison, M. J., Coe, H., et al. (2007).
816 Hygroscopic growth and water uptake kinetics of two-phase aerosol particles consisting of
817 ammonium sulfate, adipic and humic acid mixtures. *Aerosol Science*, 38, 157–171.

818 Stein, A. F., Draxler, R. R., Rolph, G. D., Stunder, B. J. B., Cohen, M. D., & Ngan, F. (2015). NOAA's
819 HYSPLIT Atmospheric Transport and Dispersion Modeling System. *Bulletin of the American*
820 *Meteorological Society*, 96, 2059–2077. Retrieved from [https://doi.org/10.1175/BAMS-D-14-](https://doi.org/10.1175/BAMS-D-14-00110.1)
821 [00110.1](https://doi.org/10.1175/BAMS-D-14-00110.1)

822 Stokes, R. H., & Robinson, R. A. (1966). Interactions in aqueous nonelectrolyte solutions. I. Solute-
823 solvent equilibria. *Journal of Physical Chemistry*, 70(7), 2126–2131.
824 <https://doi.org/10.1021/j100879a010>

825 Ström, J., Umegård, J., Tørseth, K., Tunved, P., Hansson, H. C., Holmén, K., et al. (2003). One year of
826 particle size distribution and aerosol chemical composition measurements at the Zeppelin Station,
827 Svalbard, March 2000-March 2001. *Physics and Chemistry of the Earth*, 28(28–32), 1181–1190.
828 <https://doi.org/10.1016/j.pce.2003.08.058>

829 Tanner, D. J., Jefferson, A., & Eisele, F. L. (1997). Selected ion chemical ionization mass spectrometric
830 measurement of OH. *Journal of Geophysical Research Atmospheres*, 102(5), 6415–6425.
831 <https://doi.org/10.1029/96jd03919>

832 Thompson, C. R., Shepson, P. B., Liao, J., Huey, L. G., Apel, E. C., Cantrell, C. A., et al. (2015).
833 Interactions of bromine, chlorine, and iodine photochemistry during ozone depletions in Barrow,
834 Alaska. *Atmospheric Chemistry and Physics*, 15, 9651–9679. [https://doi.org/10.5194/acp-15-9651-](https://doi.org/10.5194/acp-15-9651-2015)
835 2015

836 Tomasi, C., Lupi, A., Mazzola, M., Stone, R. S., Dutton, E. G., Herber, A., et al. (2012). An update on
837 polar aerosol optical properties using POLAR-AOD and other measurements performed during the
838 International Polar Year. *Atmospheric Environment*, 52, 29–47.
839 <https://doi.org/10.1016/j.atmosenv.2012.02.055>

840 Tremblay, S., Picard, J.-C., Bachelder, J. O., Lutsch, E., Strong, K., Fogal, P., et al. (2019).
841 Characterization of aerosol growth events over Ellesmere Island during the summers of 2015 and
842 2016. *Atmos. Chem. Phys.*, 19, 5589–5604. <https://doi.org/10.5194/acp-19-5589-2019>

843 Tunved, P., Ström, J., & Krejci, R. (2013). Arctic aerosol life cycle: linking aerosol size distributions
844 observed between 2000 and 2010 with air mass transport and precipitation at Zeppelin station, Ny-
845 Ålesund, Svalbard. *Atmospheric Chemistry and Physics*, 13(7), 3643–3660.
846 <https://doi.org/10.5194/acp-13-3643-2013>

847 Villani, P., Picard, D., Marchand, N., & Laj, P. (2007). Design and validation of a 6-volatility tandem
848 differential mobility analyzer (VTDMA). *Aerosol Science and Technology*, 41(10), 898–906.
849 <https://doi.org/10.1080/02786820701534593>

850 Virkkula, A., Van Dingenen, R., Raes, F., & Hjorth, J. (1999). Hygroscopic properties of aerosol formed
851 by oxidation of limonene, α -pinene, and β -pinene. *Journal of Geophysical Research Atmospheres*,
852 104(D3), 3569–3579. <https://doi.org/10.1029/1998JD100017>

853 Wehner, B., Philippin, S., & Wiedensohler, A. (2002). Design and calibration of a thermodenuder with an
854 improved heating unit to measure the size-dependent volatile fraction of aerosol particles. *Journal of*
855 *Aerosol Science*, 33(7), 1087–1093. [https://doi.org/10.1016/S0021-8502\(02\)00056-3](https://doi.org/10.1016/S0021-8502(02)00056-3)

856 Weingartner, E., Baltensperger, U., & Burtscher, H. (1995). Growth and Structural Change of
857 Combustion Aerosols at High Relative Humidity. *Environmental Science and Technology*, 29(12),
858 2982–2986. <https://doi.org/10.1021/es00012a014>

859 Wiedensohler, A., Covert, D. S., Swietlecki, E., Aalto, P., Heintzenberg, J., & Leck, C. (1996).
860 Occurrence of an ultrafine particle mode less than 20 nm in diameter in the marine boundary layer
861 during Arctic summer and autumn. *Tellus B*, 48(2), 213–222. [https://doi.org/10.1034/j.1600-](https://doi.org/10.1034/j.1600-0889.1996.t01-1-00006.x)
862 0889.1996.t01-1-00006.x

863 Willis, M. D., Burkart, J., Thomas, J. L., Köllner, F., Schneider, J., Bozem, H., et al. (2016). Growth of
864 nucleation mode particles in the summertime Arctic: a case study. *Atmospheric Chemistry and*
865 *Physics*, 16, 7663–7679. <https://doi.org/10.5194/acp-16-7663-2016>

866 Zheng, G., Wang, Y., Wood, R., Jensen, M. P., Kuang, C., McCoy, I. L., et al. (2021). New particle
867 formation in the remote marine boundary layer. *Nature Communications*, 12(1).

868 <https://doi.org/10.1038/s41467-020-20773-1>
869 Zieger, P., Väisänen, O., Corbin, J. C., Partridge, D. G., Bastelberger, S., Mousavi-Fard, M., et al. (2017).
870 Revising the hygroscopicity of inorganic sea salt particles. *Nature Communications*, 8.
871 <https://doi.org/10.1038/ncomms15883>
872 Ziemba, L. D., Dibb, J. E., Griffin, R. J., Huey, L. G., & Beckman, P. (2010). Observations of particle
873 growth at a remote, Arctic site. *Atmospheric Environment*, 44(13), 1649–1657.
874 <https://doi.org/10.1016/j.atmosenv.2010.01.032>
875